



UNIVERSITÀ
DEGLI STUDI
FIRENZE

FLORE

Repository istituzionale dell'Università degli Studi di Firenze

VIV mechanisms of a non-streamlined bridge deck equipped with traffic barriers

Questa è la versione Preprint (Submitted version) della seguente pubblicazione:

Original Citation:

VIV mechanisms of a non-streamlined bridge deck equipped with traffic barriers / Bernardo Nicese, Antonino Maria Marra, Gianni Bartoli, Claudio Mannini. - In: JOURNAL OF FLUIDS AND STRUCTURES. - ISSN 0889-9746. - ELETTRONICO. - (2024), pp. 1-45.

Availability:

This version is available at: 2158/1395022 since: 2024-10-06T20:08:14Z

Terms of use:

Open Access

La pubblicazione è resa disponibile sotto le norme e i termini della licenza di deposito, secondo quanto stabilito dalla Policy per l'accesso aperto dell'Università degli Studi di Firenze (<https://www.sba.unifi.it/upload/policy-oa-2016-1.pdf>)

Publisher copyright claim:

Conformità alle politiche dell'editore / Compliance to publisher's policies

Questa versione della pubblicazione è conforme a quanto richiesto dalle politiche dell'editore in materia di copyright.

This version of the publication conforms to the publisher's copyright policies.

(Article begins on next page)

Excitation mechanisms involved in the VIV of a non-streamlined bridge deck equipped with traffic barriers

Bernardo Nicese ^a, Antonino Maria Marra ^b, Gianni Bartoli ^a, Claudio Mannini ^a

^a*CRIACIV/ Department of Civil and Environmental Engineering, University of Florence, Via S. Marta, 3, Florence, Italy;*

^b*CRIACIV/Department of Architecture, University of Florence, Piazza Brunelleschi, 6, Florence, Italy;*

ABSTRACT: Although vortex-induced vibration (VIV) has been the object of research for half a century, it is still a crucial phenomenon for the design of light and flexible bridges, as it can lead to discomfort for the users and even fatigue damage. This issue has been addressed in the literature mostly for either quasi-streamlined or shallow π -deck sections, typical of long-span bridges, since the latter are particularly prone to wind-induced oscillations. Although full-scale observations demonstrate that even steel-box girder bridges, usually characterized by a shorter span length if compared to suspension and cable-stayed bridges, can experience a violent VIV response, systematic studies for these bluffer cross-section geometries are less frequent. In addition, the aerodynamic optimization of non-structural additions (barriers, screens, fairings) is rarely carried out for this bridge typology. Therefore, a wind tunnel investigation is carried out on a non-streamlined box-girder sectional model (inspired by the Volgograd Bridge, Russia) equipped with two typologies of traffic barriers giving rise to a large ratio of barrier height to deck width, considering a realistic range of angles of attack. A large and even unexpected variability in the vibration amplitude and lock-in curve pattern is found, emphasizing the existence of competing excitation mechanisms. Indeed, low-porosity barriers create a cavity on the upper side of the deck, which is known to foster the impinging-shear-layer instability, as for instance in H-shaped sections. This vortex-shedding mechanism co-exists with the dominant Kármán-vortex shedding and is responsible for a significant anticipation of the VIV onset compared to the predictions based on the Strouhal number measured during static tests. The intensity of the secondary excitation mechanism and its interaction with the dominant mechanism strongly depend on the angle of attack and is largely responsible for profound changes in the VIV bridge response. The wind tunnel results are also reconsidered in light of the quasi-steady theory, highlighting some, even qualitative, discrepancies.

32 KEYWORDS: Vortex-induced vibration; Bridge decks; Wind tunnel tests; Traffic barriers; Vor-
33 tex-shedding mechanisms; Impinging shear-layer instability

34 1 INTRODUCTION

35 The construction of light and slender bridge structures, characterized by limited mass per unit
36 length and low frequency of oscillation, has become more and more common over the years. For
37 this reason, the study of vortex-induced vibrations (VIV) of bridge decks can be crucial for the
38 structural design. Such a phenomenon is able to produce remarkable oscillations, with possible
39 fatigue damage accumulation on structural elements and travel safety and/or comfort level reduc-
40 tion for pedestrians and road or railway users.

41 The relevance of this phenomenon in bridge design is demonstrated by several well-known
42 examples of bridges suffering from VIV, such as the Great Belt East Bridge in Denmark (both the
43 suspension bridge deck and the access viaduct girder; Schewe and Larsen, 1998; Larsen et al.,
44 2000; Frandsen, 2001) or the Trans-Tokyo Bay Crossing Bridge in Japan (Fujino and Yoshida,
45 2002). A more recent and evocative case of VIV affected the Volgograd Bridge, Russia, which
46 showed large vertical vibrations in May 2010, just few months after completion, with a maximum
47 peak-to-peak amplitude of approximately 80 cm. To suppress the wind-induced oscillations, semi-
48 active tuned mass dampers were designed and installed inside the girder (Weber et al., 2013). Such
49 a VIV event had a strong echo in the media and pointed out the potentially severe effects of vortex
50 shedding not only for cable-supported decks but also for a girder bridge with shorter span length.
51 Finally, the vortex-induced oscillations observed on May 5th, 2020 in the Humen Pearl River
52 Bridge, in Guangdong province in China, also deserve a mention, since this bridge had never been
53 affected before by significant vortex-induced oscillations though it was opened in 1997. This VIV
54 event was probably promoted by the temporary installation of water-filled barriers (Ge et al.,
55 2022), with a consequent modification of bridge aerodynamics, and it is representative of the crit-
56 ical alteration of the VIV response caused by non-structural elements installed on the deck.

57 A large part of the literature about VIV refers to cylindrical bodies with paradigmatic and sim-
58 ple cross-section geometry, such as circle, square or rectangles with various side ratios. In the
59 engineering practice, the circular section is representative of a multitude of different structural
60 elements, like cables, chimneys or risers. On the other hand, square and rectangular sections are

61 largely studied in the context of wind action on tall and slender buildings, suspenders, etc. Elongated rectangular sections are also considered in several studies dealing with bridge deck VIV
62 (e.g., Ehsan & Scanlan, 1990; Matsumoto et al., 1993; Marra et al., 2011; Marra et al., 2015).
63 Nevertheless, even for similar width-to-depth ratios, bridge sections exhibit a large variety of
64 shapes, which are the result of structural and non-structural elements, both influencing the VIV
65 response.
66

67 The VIV behavior of a bridge deck is also strictly connected to the physical mechanism of
68 vortex-excitation. In this respect, Shiraishi and Matsumoto (1983) classified rectangular and bridge
69 sections in three groups based on their vortex-excited across-wind response. In particular, one of
70 them refers to moderately elongated sections, with a side ratio between approximately 2 and 7.5
71 (see also Matsumoto et al., 1993), where two kinds of unsteady vortices may coexist: one generated
72 at the leading edge due to the vibration of the body, and the other shed in the wake near the trailing
73 edge. This section typology is representative of the VIV response of elongated rectangular cylinders
74 and of a multitude of bridge decks, with an excitation related to the instability of the shear
75 layer separating at the leading edge. This mechanism is called motion-induced excitation, and it is
76 characterized by a nondimensional frequency of about 0.6, normalized with the cross-section
77 width, constant over a wide range of side ratios (Matsumoto et al., 1993). This excitation may
78 coexist with the Kármán-vortex shedding excitation, generated by the interaction of separated
79 shear layers behind the body. Nakamura described the former mechanism without invoking the
80 motion of the body (Nakamura and Nakashima, 1986). He explained the vortex excitation not
81 attributable to the Kármán-vortex trail with the impinging shear-layer instability, according to
82 which a single separated shear layer forms a vortex in presence of a sharp trailing edge, following
83 the feedback effect of it. This phenomenon is supposed to rule the shedding of vortices for rectangular
84 cylinders with a side ratio greater than about 3, H and T-shaped cross sections, and other
85 elongated bluff cylinders (see, e.g., Nakamura and Nakashima, 1986; Nakamura and Matsukawa,
86 1987; Mannini et al., 2017). According to this interpretation, the Strouhal number (also for a body
87 at rest) is constant for a wide range of side ratios and equal to about 0.6 (if normalized with the
88 cross-section width). The impinging shear-layer instability is particularly pronounced for an H-
89 shaped geometry and for the flow past cavities (Rockwell and Naudascher, 1978); the Strouhal
90 number identified by Nakamura and Nakashima (1986) takes values around 0.6 for a cavity width-
91 to-depth ratio ranging from 2 to 8. Similarly, vertical elements installed at both ends of a bridge

92 section, such as barriers or screens, may give rise to a sort of cavity on the upper side of the deck,
93 especially if they are characterized by a low porosity.

94 The side ratio and the bare deck geometry are critical factors for bridge aerodynamic and aero-
95 elastic behavior, but it is well known that nonstructural devices with either an aerodynamic or a
96 service purpose may also radically affect the VIV response. Such elements are always present in
97 bridge decks in the form of lateral traffic barriers (e.g., Kubo et al, 2002; Bai et al., 2020; Yan et
98 al., 2022), railings or parapets for pedestrians (e.g., Larsen and Wall, 2012; Hu et al., 2018), or
99 screens to protect from wind or noise (e.g., Honda et al., 1992). All of them exhibit a height that
100 is non-negligible or, in some cases, even comparable to the depth of the bare deck. Besides the
101 height, the position where these elements are installed on the bridge section (Honda et al., 1992;
102 Kubo et al, 2002), and even more the percentage and distribution of the openings (Yan et al., 2022)
103 are also very important. The distribution of open and sealed portions of a barrier may even be
104 employed to mitigate vortex-induced oscillation (Bai et al., 2020). A subset of the works men-
105 tioned above (Honda et al., 1992; Kubo et al, 2002; Bai et al., 2020) also deal with the bridge VIV
106 behavior for a certain range of wind angles of attack, since the incoming flow inclination is strictly
107 connected to the effect of screens or barriers installed on the deck.

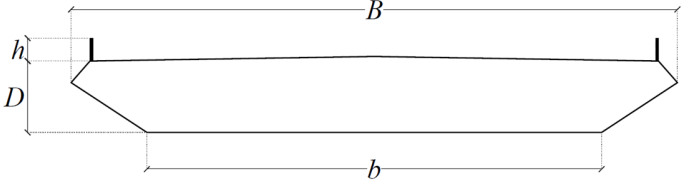
108 To provide a clearer overview of the past researches about VIV of bridge decks, which may be
109 useful not only for the present work but also as a database for future research, a collection of
110 studies available in the literature is reported in Table 1. Therein, the typology of investigation is
111 indicated, distinguishing between wind tunnel tests (WT), computational fluid dynamics simula-
112 tions (CFD) and full-scale measurements (FS). The typologies of bridge and deck section are also
113 reported, along with the ratios of some relevant geometric quantities: B is the total width of the
114 cross section, while b denotes the width of the horizontal part of the lower side of the deck; D is
115 the depth of the bare deck; h is the height of the vertical barriers or screens installed on the bridge.
116 A graphical comparison between the bridge sections collected in Table 1 is also provided in terms
117 of ratios between cross-section dimensions (Fig. 1(a)) and normalized barrier height (Fig. 1(b)). In
118 particular, the ratio h/B characterizes the geometry of the cavity created on the deck upper side by
119 a pair of lateral barriers or screens; especially for a low porosity of them, this ratio may be crucial
120 for the vortex-shedding mechanism associated with impinging shear-layer-instability (or motion-
121 induced excitation). The peak transverse amplitude of vibration Y_{peak} , normalized with D , and the
122 corresponding mass-damping parameter, the Scruton number (Sc), are also reported in Table 1.

123 The Scruton number is evaluated as $Sc = 4\pi m\zeta_0/\rho BD$, where m is the mass per unit length, ζ_0 is the
124 structural damping, and ρ is the air density. Most of the studies collected in Table 1 deal with the
125 VIV response of elongated or quasi-streamlined bridge deck sections, typical of long-span bridges,
126 which usually draw the attention of researchers due to their sensitivity to wind-induced excitation.
127 Some studies dealing with π -shaped deck sections are also included in Table 1; this section typol-
128 ogy is often adopted for cable-stayed bridges and, despite the poor aerodynamic performance (es-
129 pecially in the absence of fairings), it is usually characterized by a fairly large ratio of along-wind
130 to across-wind dimensions. The lowest B/D ratios in Table 1, lower than 4, are those associated
131 with the Rio-Niterói Bridge (Battista and Pfeil, 2000), the Deer Isle Bridge (Kumarasena et al.,
132 1991), the approaching spans of the Great Belt East Bridge (Larsen et al., 1995; Schewe and
133 Larsen, 1998), and the Trans-Tokyo Bay Crossing Bridge (Fujino and Yoshida, 2002). Except for
134 the Deer Isle Bridge, which is a suspension bridge with an open section, the others are girder
135 bridges with a non-streamlined steel box section. Their maximum span length ranges from about
136 200 m to 250 m, and they exhibited remarkable peak transverse amplitude of vibration, between
137 4% and 10% of D at full scale and during wind tunnel tests. A slightly larger side ratio characterizes
138 the Volgograd Bridge, which presents a bluff trapezoidal box girder with lateral cantilevers (Cor-
139 riols and Morgenthal, 2012). This case study is meaningful, since it experienced the most violent
140 VIV event collected in Table 1, although the deck girder is characterized by the shortest span
141 length (155 m) among those reported there. It is also worth noting that this bridge exhibits a high
142 ratio of the barrier height to the deck depth (h/D) and width (h/B), which is expected to have an
143 impact on the possible excitation due to impinging shear-layer instability. The analysis of Table 1
144 suggests that the literature lacks studies of the VIV behavior of box cross sections characterized
145 by low side ratios and relatively high barriers, typical of girder bridges with an important span
146 (though noticeably shorter than those of cable-supported bridges). In addition, due to the non-
147 streamlined deck profile and the relatively limited span length, the aerodynamic performances of
148 non-structural additions like barriers or screens are frequently considered of minor importance for
149 this bridge typology and rarely optimized from the aerodynamic point of view. Finally, most of
150 the collected literature contributions are limited to the null angle of attack, despite the well-known
151 importance of this parameter.

152 Based on these considerations, in the present work a wide experimental campaign is performed
153 on a sectional model presenting a realistic and relatively bluff geometry, inspired by the Volgograd

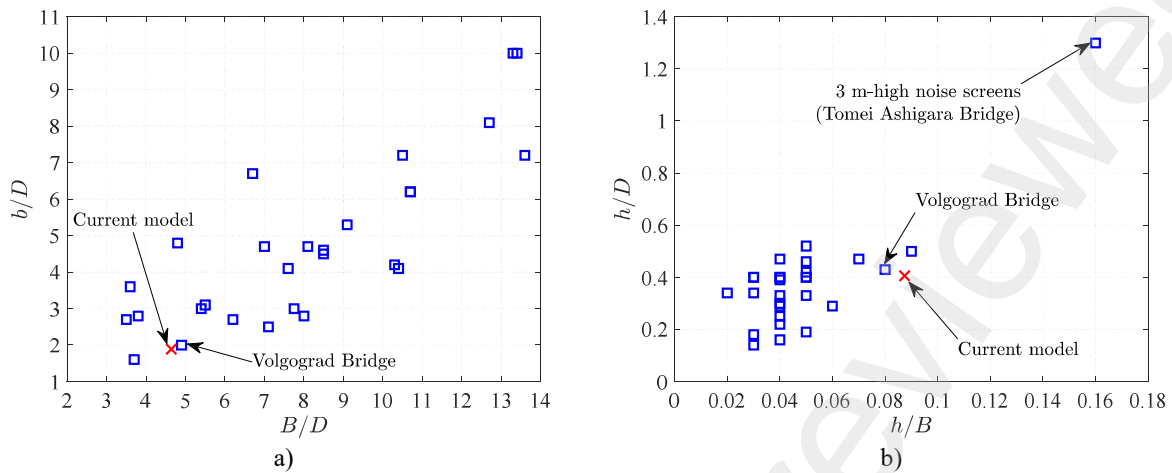
154 Bridge deck and having large traffic barriers compared to the depth and, above all, to the width of
155 the deck section (see Fig. 1). The aerodynamic effects of two different typologies of lateral traffic
156 barriers are evaluated by means of static force measurements and aeroelastic tests. Wake measure-
157 ments behind both the stationary and the vibrating model are also performed in some cases, to
158 better understand the VIV response. The study is carried out over a range of angles of attack typical
159 of practical applications. The experiments aim to shed some light on the different vortex-induced
160 excitation mechanisms and their possible interaction or interference, which is an aspect that is
161 usually not dealt with for bridge sections equipped with realistic additions. In particular, attention
162 is paid to the influence of the barriers not only on the VIV response amplitude, but also on the
163 onset and extension of the lock-in regime, always keeping in mind literature results for more ge-
164 neric and paradigmatic cross sections (e.g., rectangular and H-shaped sections). The accuracy of
165 the quasi-steady theory in predicting potential galloping instabilities of the considered bridge
166 model is also ascertained.

Table 1. Collection of VIV studies.



Bridge	Reference	Study	Deck section	Bridge typology	Span length [m]	B/D	b/D	h/D	h/B	α [°]	Y_{peak}/D	Sc
Chongqing Hechuan Bridge	Bai et al. (2020)	WT	Streamlined box girder	Suspension	400	7.6	4.1	0.4	0.05	-3 to 3	0.07	12.3
Deer Isle Bridge	Kumarasena et al. (1991)	FS	H-shaped section	Suspension	329	3.6	3.6	0.68	0.19	-	0.02	-
Great Belt East Bridge (suspended span)	Larsen (1993)	WT	Streamlined box girder	Suspension	1624	7	4.7	0.33	0.05	0	0.06	-
Great Belt East Bridge (approaching spans)	Larsen et al. (1995)	WT	Trapezoidal box girder	Steel girder	193	3.7	1.6	0.18	0.05	0	0.11	5.6
	Schewe and Larsen (1998)	FS								-	0.02	-
Haihe Bridge	Meng et al. (2011)	WT CFD	Trapezoidal box girder	Cable-stayed	310	8.1	4.7	0.4	0.05	0	0.10	11.9
Hålogaland Bridge	Larsen and Wall (2012)	WT	Streamlined box girder	Suspension	1145	6.2	2.7	0.47	0.07	0	0.04	6.2
Hong Kong-Zhuhai-Macao Bridge	Chen et al. (2017)	WT	Elongated trapezoidal box girder with lateral cantilevers	Cable-stayed	258	8.5	4.5	0.25	0.04	-5 to 5	0.12	7.7
Humen Bridge	Ge et al. (2022)	FS	Streamlined box girder	Suspension	888	13.3	10	0.4	0.03	-	0.12	13.2
Jindo Bridge	Seo et al (2013)	FS	Trapezoidal box girder	Cable-stayed	340	1 st bridge				-	0.13	-
						2 nd bridge						
						parallel layout						
Kessock Bridge	Owen et al. (1996)	WT	Open π -shaped section	Cable-stayed	240	6.7	6.7	0.29	0.04	0	0.05	-
Osteroy Bridge	Larsen and Wall (2012)	WT	Streamlined box girder	Suspension	595	5.4	3	0.5	0.09	0	0.04	5.4
Qingshan Yangtze River Bridge	Li et al. (2018)	WT	Streamlined box girder	Cable-stayed	938	10.4	4.1	0.34	0.03	-5 to 5	0.07	8.1
Rio-Niterói Bridge	Battista and Pfeil (2000)	WT	Rectangular box girder	Steel girder	300	3.5	2.7	0.19	0.05	0	0.04	-
Second Severn Crossing Bridge	Macdonald et al. (2002)	WT	Open π -shaped section	Cable-stayed	456	10.7	6.2	0.40	0.04	0	0.07	1.0
		FS								-	0.06	-
Stonecutters Bridge	Larose et al. (2003)	WT	Streamlined twin-box girder		1018	13.6	7.2	0.40	0.03	-	0.14	-

	Larsen et al. (2008)			Cable-stayed									
Sunshine Skyway Bridge	Ricciardelli et al. (2002)	WT	Elongated trapezoidal box girder with lateral cantilevers	Cable-stayed	364	7.1	2.5	0.18	0.03	0	0.01	-	
Tacoma Narrows Bridge	Matsumoto et al. (2003)	WT	H-shaped section	Suspension	853	4.8	4.8	0.29	0.06	0	0.27	5.0	
Tomei Ashigara Bridge	Honda et al. (1992)	WT	Streamlined box girder	Cable-stayed	185	8	2.8	1.3	0.16	-4 to 8	0.08	0.9	
Trans-Tokyo Bay Crossing Bridge	Fujino and Yoshida (2002)	WT	Rectangular box girder with lateral cantilevers	Steel girder	240	3.8	2.8	0.14	0.03	-3 to 3	0.09	-	
		FS								-	0.08	-	
	Sarwar and Ishihara (2010)	CFD								0	0.07	1.6	
Volgograd Bridge	Corriols and Morgenthal (2012)	CFD	Trapezoidal box girder with lateral cantilevers	Steel girder	155	4.9	2	0.43	0.08	-	0.23	-	
Xiangshan Harbor Bridge	Zhu et al. (2013)	WT	Streamlined box girder	Cable-stayed	688	9.1	5.3	0.42	0.05	0	0.09	9.1	
Yi Sun-Shin Bridge	Hwang et al. (2019)	FS	Streamlined twin-box girder	Suspension	1545	10.3	4.2	0.39	0.04	0	0.09	4.7	
Generic bridge sections	Kubo et al. (2002)		Open π -shaped section			10	-	0.4	0.04	-6 to 6	0.15	4.7	
	Larsen and Wall (2012)		Streamlined box girder			7.75	3	0.3	0.04	0	0.09	7.75	
	Hu et al. (2018)	WT	Streamlined box girder			10.7	6.2	0.46	0.05	0	0.07	10	
	Sun et al. (2019)		Streamlined box girder	-	-	8.5	4.6	0.33	0.04	0 to 5	0.12	9.3	
	Wang et al. (2020)		Streamlined box girder			10.5	7.2	0.52	0.05	0 to 7	0.05	5.6	
	Yan et al. (2022)		Hexagonal box girder			5.5	3.1	0.22	0.04	0	0.20	7.7	
	Wang et al. (2023)	CFD	Streamlined box girder			13.4	10	0.34	0.02	-3 to 3	0.37	6	



169 Fig. 1. Comparison between the bridge sections collected in Table 1 and the current sectional model in terms of B/D
 170 against b/d (a) and of h/B against h/D (b).
 171

172 2 WIND TUNNEL EXPERIMENTS

173 2.1 Wind tunnel facility and model

174 The tests are carried out in the open-circuit boundary layer wind tunnel of CRIACIV (Inter-
 175 University Research Centre on Building Aerodynamics and Wind Engineering), located in Prato,
 176 Italy. The closed rectangular test section is 2.42 m wide and 1.60 m high. The flow is drawn by a
 177 156-kW fan, and its speed can be continuously varied in the range 0–30 m/s, with a free-stream
 178 turbulence intensity below 1%. Temperature and atmospheric pressure are constantly monitored
 179 with a probe to calculate the air density.

180 A bridge deck sectional model is employed for both static and aeroelastic tests, with a cross
 181 section inspired by the Volgograd Bridge, in Russia. This bridge is characterized by a slightly non-
 182 symmetric cross section, with two lateral cantilevers of different length jutting out from a trape-
 183 zoidal steel box girder (Corriols and Morgenthal, 2012). Such a length difference comes from the
 184 presence of a walkway only on one of the two sides of the section. In contrast, the cross section of
 185 the wind tunnel model is symmetric, aiming at a more paradigmatic deck geometry and, hence, at
 186 a greater generality of the work.

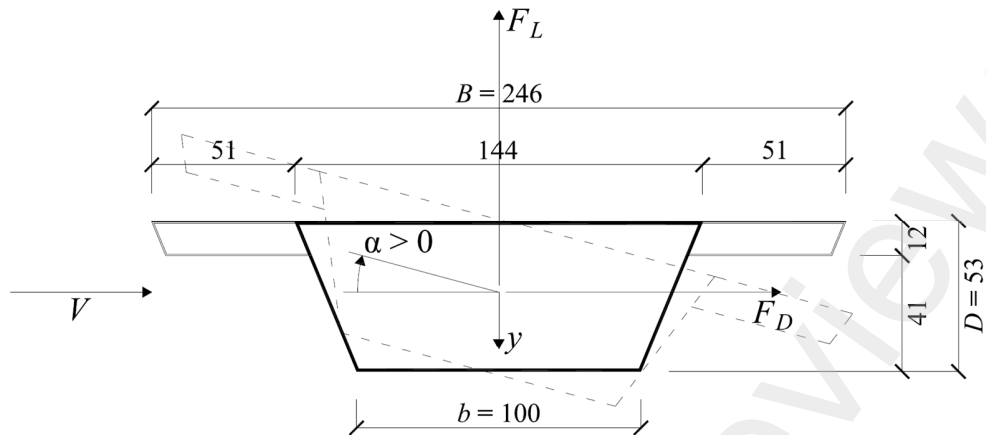
187 Fig. 2 shows a schematic representation of the model cross section. F_D and F_L denote respec-
 188 tively the drag and lift forces, V is the wind velocity, and α is the angle of attack (positive nose

189 up). The sectional model is 1000 mm long (L), its upper and lower widths are respectively 246
190 mm (B) and 100 mm (b), while the across-flow size is 53 mm (D), referring to the bare deck layout.
191 The resulting cross-section side ratios are $B/D = 4.6$ and $b/D = 1.9$. The box girder is realized with
192 a 1 mm-thick aluminum plate, and a 0.5 mm-thick upper horizontal plate is fixed on the top of the
193 girder, supported by lateral ribs on both sides. Internal ribs in the trapezoidal core of the model are
194 also employed to avoid model deformation. The model lower corners are made sharp using a two-
195 component adhesive paste (Fig. 3(a)). To promote two-dimensional flow conditions, aluminum
196 rectangular end-plates (500 mm \times 210 mm, having a thickness of 2 mm for the static tests and 1
197 mm for the dynamic tests) are provided at both ends of the model. Including the light end-plates,
198 the model has a mass of 2.81 kg.

199 Two realistic typologies of bridge lateral barriers are installed on the model (Fig. 3(b-e)). They
200 are made of aluminum and present nearly the same height but a different degree of transparency
201 to the flow: the first one (Barrier 1) is 21 mm high, while the second one (Barrier 2) is 22 mm
202 high; their porosity is 51 % and 23 %, respectively. The largest blockage ratio (conservatively
203 calculated as the total depth of the model in the direction perpendicular to the wind divided by the
204 height of the test chamber) is 6.8 %, obtained during static force measurements for the model
205 equipped with barriers at an angle of attack of about 12° . Nevertheless, most of the tests discussed
206 in the present paper refer to an angle of attack ranging between -3° and 3° , and in these cases the
207 maximum blockage ratio is equal to 5.3 %, which is generally considered acceptable.

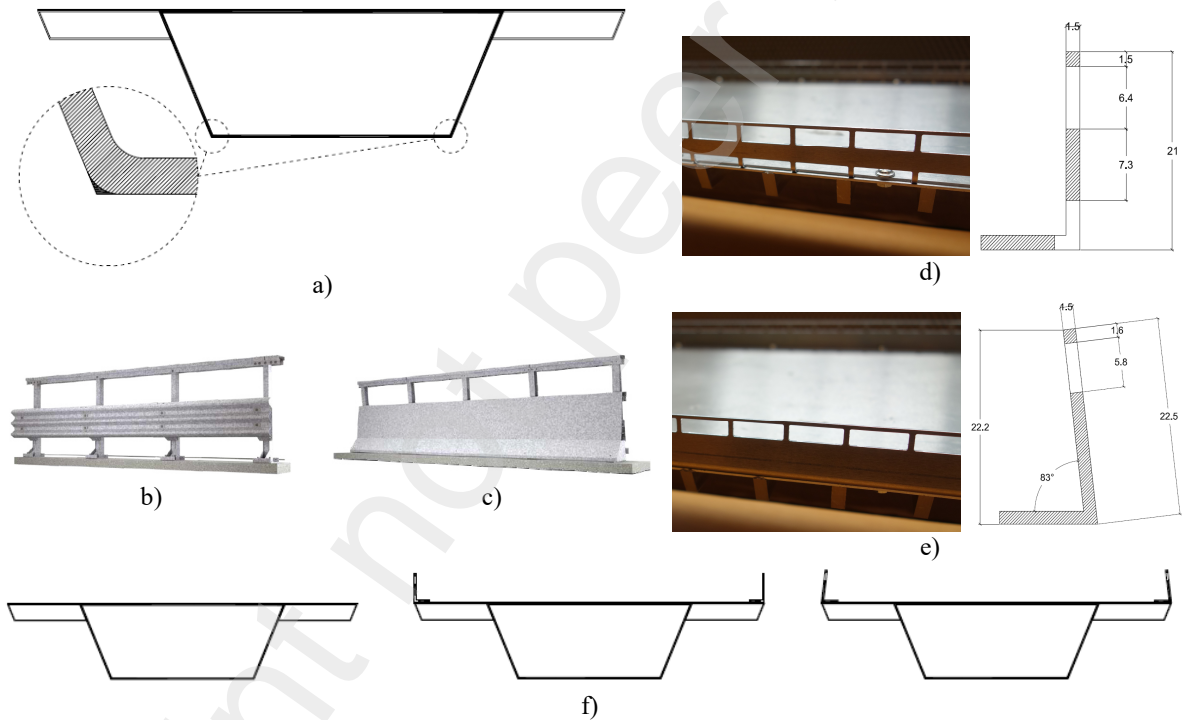
208 Finally, it is worth remarking that Barrier 1 is quite similar to the one installed on the Volgograd
209 Bridge on the side opposite to the walkway. On the other hand, Barrier 2 is representative of par-
210 tially sealed traffic barriers employed to increase the safety of the motorcyclists on the road, espe-
211 cially when cornering. It may also be representative of other cases in which weakly porous vertical
212 elements or sealed up to a considerable height are installed on the deck. For example, such a geo-
213 metric condition may occur for pedestrian parapets made of glass or similar materials.

214



215
216 Fig. 2. Sketch of the sectional model cross section (dimensions in mm). Positive drag, lift and angle of attack are also
217 indicated.

218



219 Fig. 3. Lower corner shape variation (a), Barrier 1 (b) and Barrier 2 (c). Close-up and main dimensions (in mm) of the
220 first (d) and the second (e) lateral barrier installed on the sectional model during the tests. Section layouts without
221 barriers (left), with Barrier 1 (center) and with Barrier 2 (right) are also reported (f).
222

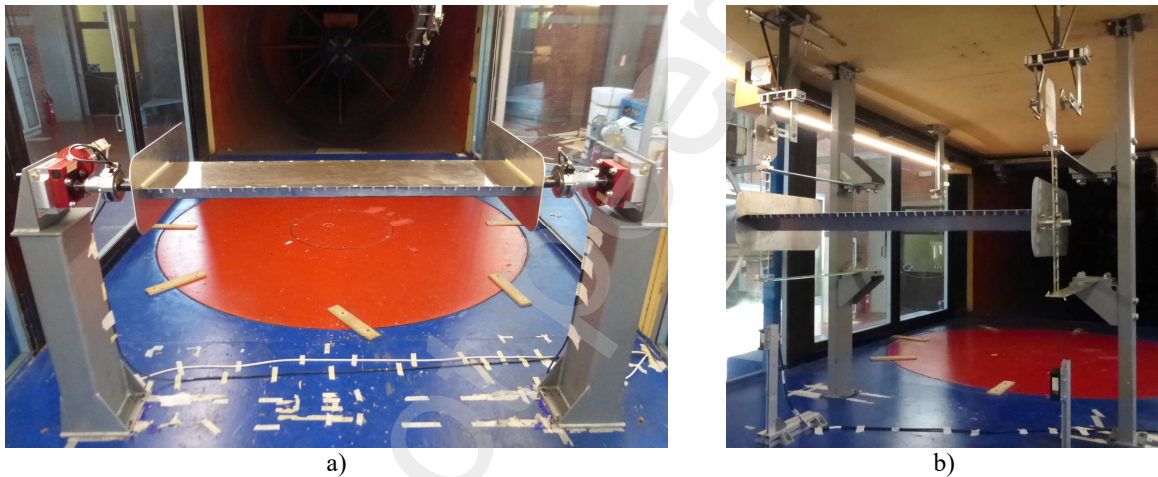
223 2.2 Experimental setups

224 Static force measurements are performed by rigidly connecting the sectional model at both ends
225 to two ATI FT-Delta SI-165-15 six-component high-frequency force balances (Fig. 4(a)). Each

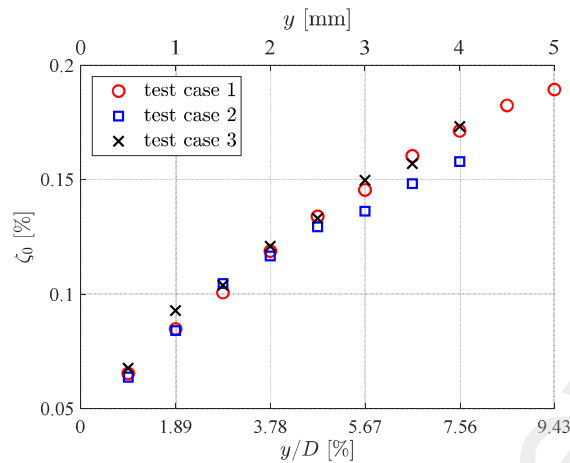
226 balance is fixed to an electric motor allowing the automatic rotation of the sectional model around
227 its longitudinal axis, so as to vary accurately the value of the angle of attack. The whole mechanism
228 is supported by two steel columns fixed to the floor of the wind tunnel. The natural frequency of
229 the system composed by the model installed on the setup for static force measurements is about
230 25 Hz.

231 Aeroelastic tests are conducted by elastically suspending the model through two shear-type
232 steel frames, connected to the longitudinal axis of the model (Fig. 4(b)). The horizontal elements
233 of the frames work as leaf springs. Only the vertical transverse displacement of the model is al-
234 lowed, because of the very high in-plane bending stiffness of the vertical Vierendeel-type girder
235 located between the horizontal plates and rigidly connected to the sectional model. The displace-
236 ments of the sectional model are recorded with two non-contact laser transducers Micro-epsilon
237 OptoNCDT 1605, located below both ends of the model. The mechanical damping of the system
238 is varied through a device based on the electro-magnetic induction principle. It consists of two
239 aluminum thin plates (250 mm × 120 mm × 2 mm), each one fixed to the end of a plate-spring and
240 moving between two pairs of magnetic disks with a diameter of 60 mm and a thickness of 5 mm
241 (Fig. 4(b)). The development of eddy currents in the aluminum plates generates the viscous damp-
242 ing force in the oscillating system. The amount of damping is controlled by finely tuning the dis-
243 tance between the magnets. The frequency (n_0) and the mechanical damping ratio (ζ_0) of the oscil-
244 lating system are measured through free-decay tests. Dynamic system identification is repeated
245 several times for each series of aeroelastic measurements, showing very good repeatability. The
246 effect of still-air resistance is minimized by considering only small vibrations for damping estima-
247 tion, namely a maximum amplitude below 0.5 mm. Nevertheless, the damping ratio of the system
248 is also evaluated for larger oscillation amplitudes, up to values comparable to those expected dur-
249 ing the aeroelastic tests (see Section 3.2). Damping is identified through the MULS method (Bar-
250 toli et al., 2009) over time windows varying from $T \approx 5$ s for the lowest amplitude to $T \approx 2$ s for
251 the largest one (i.e., n_0T approximately between 15 and 45) and is associated with the maximum
252 displacement in the window. Fig. 5 compares the results for three damping identifications: increas-
253 ing the oscillation amplitude by a factor of 10, the damping ratio increases by more than a factor
254 of two, mainly due to the still-air resistance. Since this effect does not linearly superpose to that of
255 the airflow, in the reminder of the paper we will always refer to the damping values determined
256 for small oscillation amplitudes, bearing in mind, however, that there is some uncertainty in the

257 estimation of this important set-up parameter. The effective mass of the oscillating system (M) is
258 evaluated through the addition to the system of a set of known masses and the consequent identi-
259 fication of vibration frequencies. An effective mass of 5.9 kg is estimated for the bridge deck
260 sectional model (excluding the aluminum plates of the dampers and the lateral barriers installed
261 on the bridge deck model). This result is confirmed by the static measurement of the stiffness of
262 the system (17.4 kN/m). Furthermore, the linear elastic behavior of the plate springs is verified up
263 to the highest amplitudes observed during the experimental tests. Finally, in the experimental tests
264 the natural frequency of the vibrating system ranges from 8 to 9 Hz, while the Scruton number,
265 calculated as $Sc = 4\pi M\zeta_0/\rho BDL$ (where ζ_0 refers to the damping in still air for small oscillation
266 amplitude), varies from about 3.5 to about 60.
267



268 Fig. 4. Wind tunnel setup for static force measurements (a) and for aeroelastic tests (b).
269



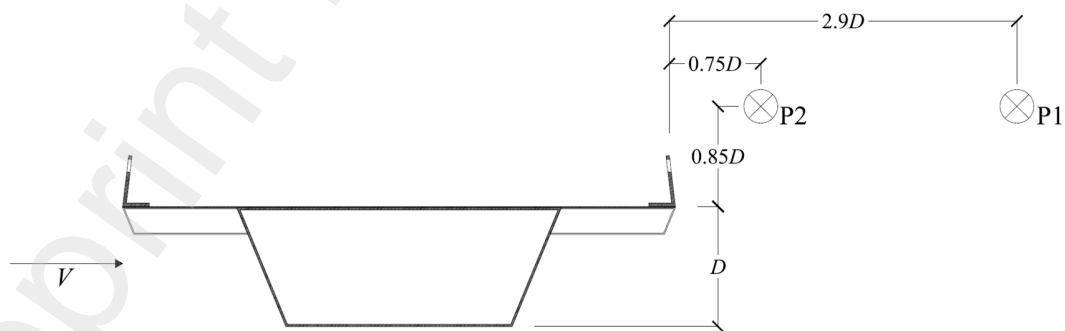
270

271 Fig. 5. Comparison between three damping-ratio identifications for different values of the oscillation amplitude (de-
 272 noted as y) in still air.

273

274 Finally, flow-velocity measurements are performed through a hot-wire anemometer installed
 275 on a robotic arm, able to move in all directions inside the test chamber behind the sectional model.
 276 The measurements are carried out with the model mounted on the aeroelastic setup (Fig. 4(b)) and
 277 they are performed both in static and dynamic conditions. In particular, for the former, the two
 278 shear-type steel frames supporting the model are restrained by a diagonal aluminum element inside
 279 the frame and by a cable connected to the floor of the wind tunnel, so preventing any vibration of
 280 the system. Fig. 6 provides the layout of the setup for the wake measurements; the probe is placed
 281 in two different positions, either at a distance of $2.9D$ downstream of the model (position P1) or
 282 much closer to the leeward barrier, at a distance of $0.75D$ from it (position P2). In both cases, the
 283 probe is located about $0.85D$ above the upper side of the deck.

284

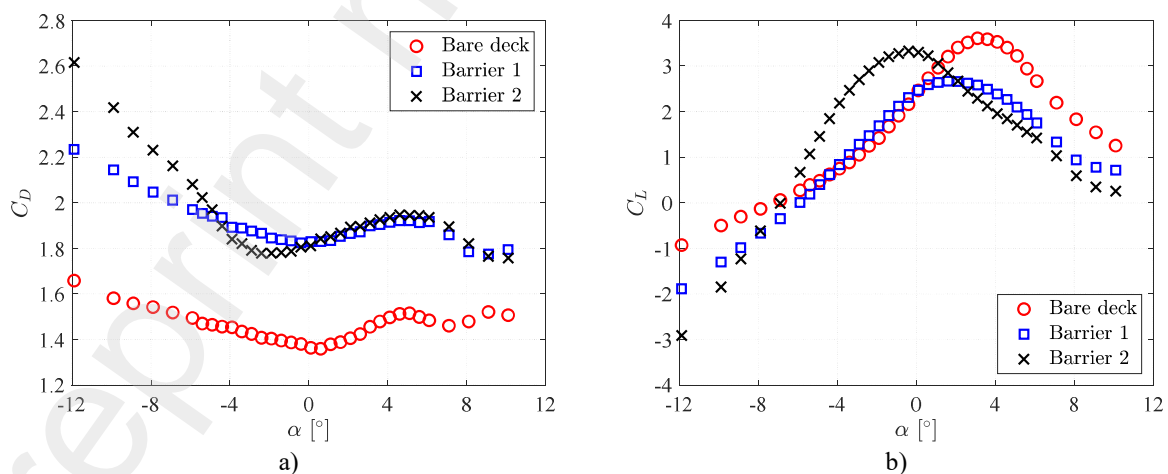


285

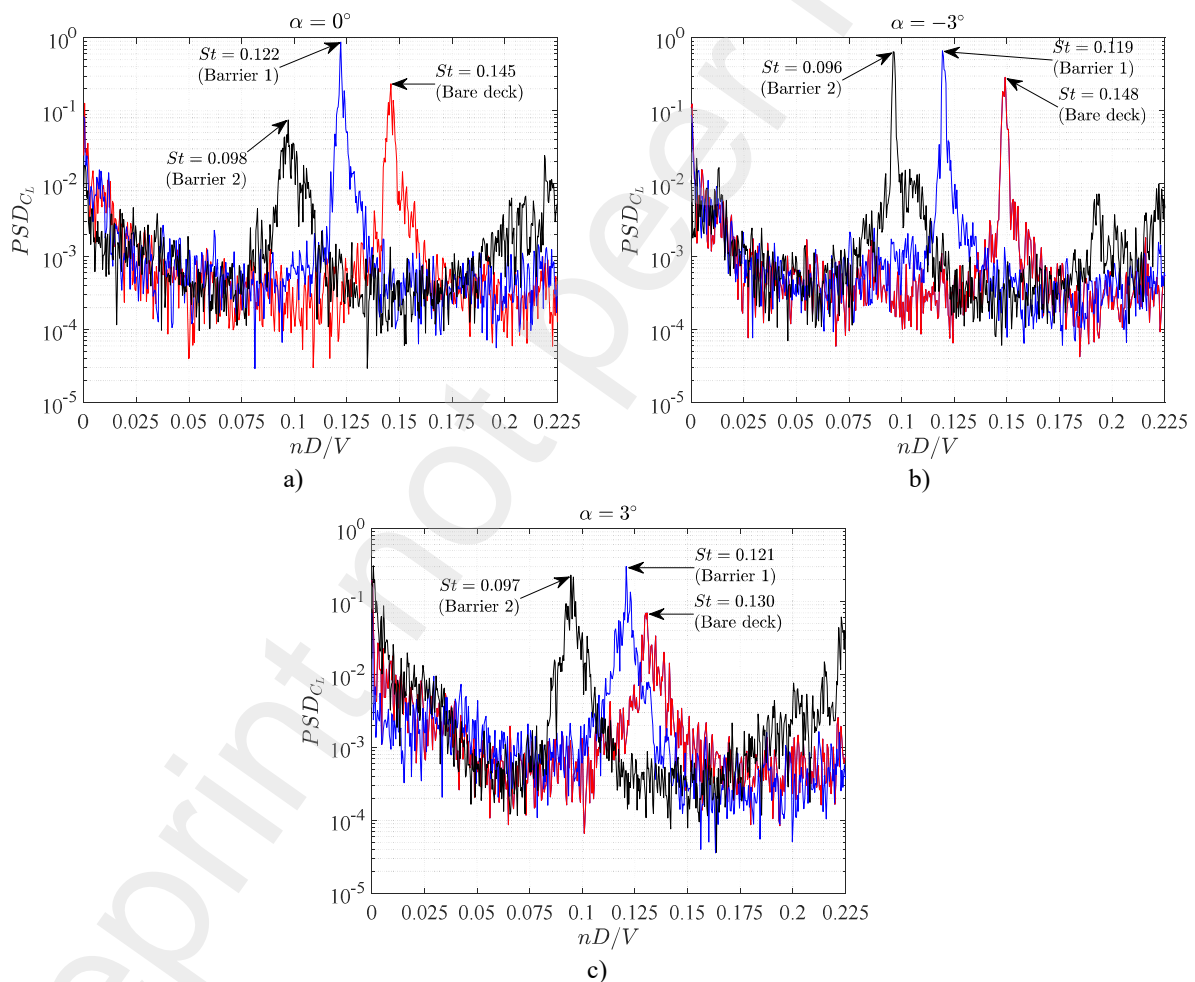
286 Fig. 6. Sketch of the bridge deck sectional model with the indication of the positions P1 and P2, where the hot-wire
 287 probe is placed to perform wake measurements.

289 3.1 Static force measurements

290 The static force measurements are carried out with the purpose of describing the aerodynamic
 291 behavior of the bridge deck section and supporting the discussion of the VIV response in the aero-
 292 elastic tests. In a first phase, the mean values of drag (F_D) and lift (F_L) forces are measured. Aero-
 293 dynamic drag (C_D) and lift coefficient (C_L) are obtained, respectively, from F_D and F_L divided by
 294 $1/2\rho V^2 LD$, where ρ is the air density. Fig. 7 shows drag and lift coefficients as functions of the
 295 angle of attack, for the sectional model with and without lateral barriers, for a Reynolds number
 296 ($Re = VD/\nu$) of about 100,000. As expected, the clearest effect of the barriers is a marked growth
 297 of the drag coefficient over the whole range of angles of attack. For positive angles, both barriers
 298 give rise to similar drag curves, while for negative angles the different porosity and distribution of
 299 the openings produce different trends of the coefficient. The peculiar drag coefficient pattern for
 300 the three deck layouts between 0° and 10° (exhibiting a bump between 5°) has been explained by
 301 flow visualizations through wool tufts attached to the sectional model (Nicese, 2021). For the bare
 302 deck, the lift coefficient (Fig. 7(b)) exhibits a positive slope up to about $\alpha = 4^\circ$, followed by a
 303 marked decreasing trend. The installation of Barrier 1 causes a decrease of the maximum lift value,
 304 and the peak is shifted towards lower values of α . With Barrier 2, the peak value of C_L is larger
 305 than for Barrier 1, and it is reached for an even lower angle of attack, very close to zero. Overall,
 306 the presence of the barriers makes more linear and steep the lift curve prior to the stall.

307 Fig. 7. Mean drag (a) and lift (b) coefficients for the sectional model with and without barriers ($Re = 100,000$).

308 Moreover, the lift fluctuations are investigated in terms of Strouhal number (St) and dimension-
 309 less amplitude of the vortex-shedding force (C_{L0}), for the purpose of making a first estimate of the
 310 proneness of the bridge section to vortex-induced vibration. The Strouhal number ($St = n_s D/V$) is
 311 determined from the frequency n_s associated with the dominant peak in the lift force spectrum.
 312 Fig. 8 shows the power spectral density of the lift coefficient at null, -3° and 3° angle of attack for
 313 the three cross-section layouts considered. These angles of attack are usually considered repre-
 314 sentative of a multitude of realistic cases, in absence of extreme orographic features of the bridge
 315 site. The Strouhal frequency reduces in presence of the lateral barriers (in particular, for Barrier 2)
 316 and both the broadness and the height of the peak are remarkably affected by the presence and the
 317 typology of the traffic barrier.



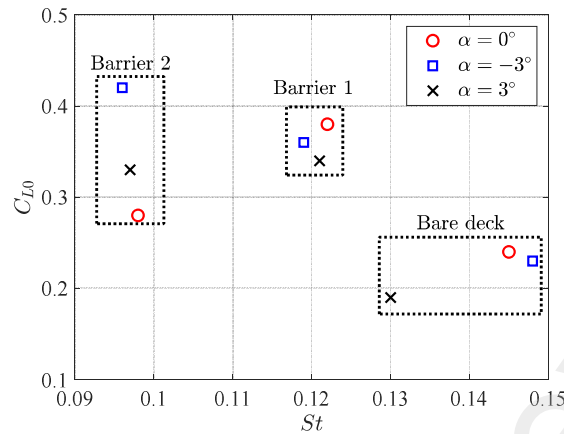
318 Fig. 8. Power spectral density of the lift coefficient at 0° , -3° and 3° flow angle of attack with and without lateral
 319 barriers ($Re = 19,000$). The spectral peaks corresponding to the Strouhal frequency are indicated.
 320

321 The coefficient C_{L0} is obtained as sinusoidal equivalent amplitude based on the integration of
 322 the lift coefficient spectrum in a narrow frequency band fully embedding the Strouhal peak. An
 323 issue is the amplification of the measured fluctuating force close to the natural frequency of the
 324 static test setup. For this reason, C_{L0} is measured keeping the Strouhal frequency sufficiently below
 325 the resonance condition; moreover, the mechanical admittance function of the system is estimated
 326 with the purpose of removing any possible amplification effects on C_{L0} (see Nicese, 2021, for
 327 further details). Table 2 reports the obtained values of the Strouhal number and C_{L0} coefficient for
 328 the three configurations and for the three angles of attack. The same values are also presented
 329 graphically by Fig. 9 and they refer to a fairly low value of the Reynolds number (about 19000),
 330 close to that at which aeroelastic tests are carried out. It is apparent that the presence of the barriers
 331 enhances vortex shedding. C_{L0} is particularly large for Barrier 1 at $\alpha = 0^\circ$ and -3° , and for Barrier
 332 2 at $\alpha = -3^\circ$. In contrast, vortex shedding is only slightly stronger than for the bare deck when
 333 Barrier 2 is installed at $\alpha = 0^\circ$.

334
 335 Table 2. Strouhal number and amplitude of the vortex-shedding force for each configuration considered and for vari-
 336 ous angles of attack ($Re = 19,000$).

	α [°]	St [-]	C_{L0} [-]
Bare deck	0	0.145	0.24
	-3	0.148	0.23
	3	0.130	0.19
Barrier 1	0	0.122	0.38
	-3	0.119	0.36
	3	0.121	0.34
Barrier 2	0	0.098	0.28
	-3	0.096	0.36
	3	0.097	0.33

337



338

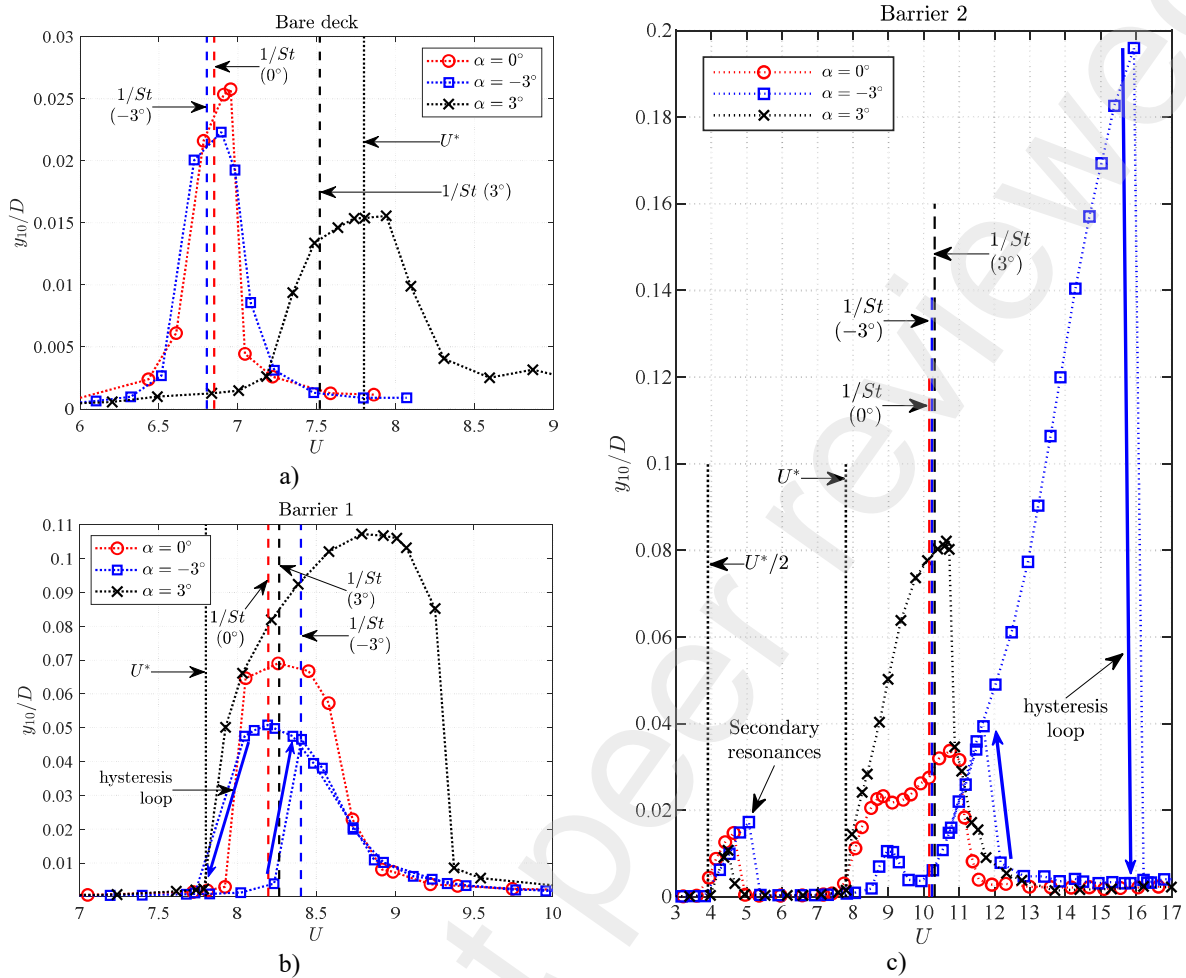
339 Fig. 9. Amplitude of the vortex-shedding lift coefficient against Strouhal number for the tested layouts at different
 340 angle of attack values ($Re = 19,000$).

341 3.2 Aeroelastic tests

342 Aeroelastic tests are performed to determine the transverse VIV response of the bridge sectional
 343 model with and without lateral barriers at different angles of attack. The sectional model is let free
 344 to oscillate for increasing values of the wind velocity. In some cases, the measurements are also
 345 performed by decreasing the flow velocity to identify possible hysteresis effects in the lock-in
 346 range. Fig. 10 shows the response curves obtained for the lowest Scruton number tested, between
 347 about 3 and 4. For the bare deck, larger positive values of the flow angle of incidence are also
 348 tested, even if not reported in the present work (see Nicese, 2021). Results are plotted in terms of
 349 non-dimensional vibration y_{10}/D , where y_{10} is evaluated as the mean value of the 10%-highest
 350 peaks in the transverse displacement time history, against reduced flow velocity $U = V/n_0D$. Vor-
 351 tex-resonance reduced velocity based on static tests ($1/St$) is also indicated in the figure, along with
 352 the theoretical reduced velocity of motion-induced excitation/impinging shear-layer instability,
 353 calculated as $U^* = (B/D)/0.6$. In addition, secondary resonances and hysteresis effects, where rel-
 354 evant, are highlighted.

355 The bare deck gives rise to moderate vibration amplitudes and synchronization ranges for -3°
 356 $\leq \alpha \leq 3^\circ$ (Fig. 10(a)). In particular, the lock-in curves at 0° and -3° are very similar to each other,
 357 with a narrow and nearly symmetric shape around the resonance velocity $1/St$. For $\alpha = 3^\circ$, the lock-
 358 in range slightly expands, and the peak response decreases from about $0.025D$ to $0.015D$.

359

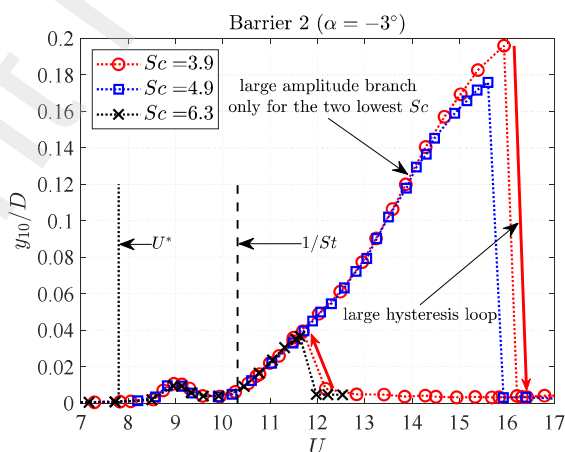


360 Fig. 10. Response curves at low Scruton number ($3 \leq Sc \leq 4$) for the bare deck (a), the deck equipped with Barrier 1
 361 (b) and Barrier 2 (c) at different angles of attack (0° , -3° , 3°).

362 With the barriers, the variability of the VIV response markedly increases for the investigated
 363 angles of attack. In the case of Barrier 1 (Fig. 10(b)), the growth of the vibration amplitude is
 364 apparent. For a null angle of attack, the synchronization range slightly widens, while the oscillation
 365 amplitude increases up to $0.07D$, which is almost three times the one experienced by the bare deck.
 366 For $\alpha = -3^\circ$, the maximum oscillation amplitude reaches a value of $0.05D$, with a hysteresis loop
 367 at the lower bound of the lock-in range. For $\alpha = 3^\circ$, the lock-in range becomes much wider, and
 368 the peak amplitude exceeds $0.1D$. A certain increase in oscillation amplitude compared to the bare
 369 deck configuration was expected based on the measured coefficient C_{L0} (Table 2); nevertheless,
 370 other aeroelastic effects must clearly come into play to justify the severe intensification of the
 371 response.

Barrier 2 produces wide lock-in ranges (Fig. 10(c)), but the peak vibration amplitudes are lower than for Barrier 1 for $\alpha = 0^\circ$ and $\alpha = 3^\circ$. In contrast, the results dramatically change for $\alpha = -3^\circ$: a very large response is observed, with a wide hysteresis loop and an upper branch reaching almost $0.2D$. Nevertheless, such a high response is found only for low Scruton numbers, as the hysteresis loop and the upper branch already disappear for $Sc = 6.3$ (Fig. 11). Once again, static tests revealed that vortex shedding is strongest for $\alpha = -3^\circ$, but the measured value of C_{L0} (Table 2) does not justify such a large response increase. In addition, Barrier 2 promotes a peculiar shape of the lock-in curve for $\alpha = 0^\circ$ and $\alpha = -3^\circ$; indeed, a local peak in the response is evident before the growth to the maximum value. It is also worth noting that the lock-in onset for all the curves associated with Barrier 2 occurs for a reduced velocity which is significantly lower than $1/St$ (based on static tests) and close to U^* . Finally, with Barrier 2 a weaker secondary resonance response occurs around $U^*/2$, as is typical for the impinging shear-layer instability excitation mechanism at low Scruton number (Schewe, 1989; Marra et al., 2015).

Fig. 12 summarizes the results for all the bridge section layouts for $-3^\circ \leq \alpha \leq 3^\circ$ and various Scruton numbers (see Table 3). The impact of the Scruton number on vibration amplitude and lock-in range slightly changes from one layout to another; the sharpest impact of the Scruton number is observed for Barrier 2 at $\alpha = -3^\circ$, for which, as previously said, the oscillation amplitude does not decrease gradually with Sc but sharply drops for a slight change of the mass-damping parameter from 4.9 to 6.3 (Fig. 11). In addition, except for this latter case, the lock-in curve pattern changes with the barrier type and with the flow angle of incidence, but it does not exhibit noticeable qualitative modifications due to the Scruton number.

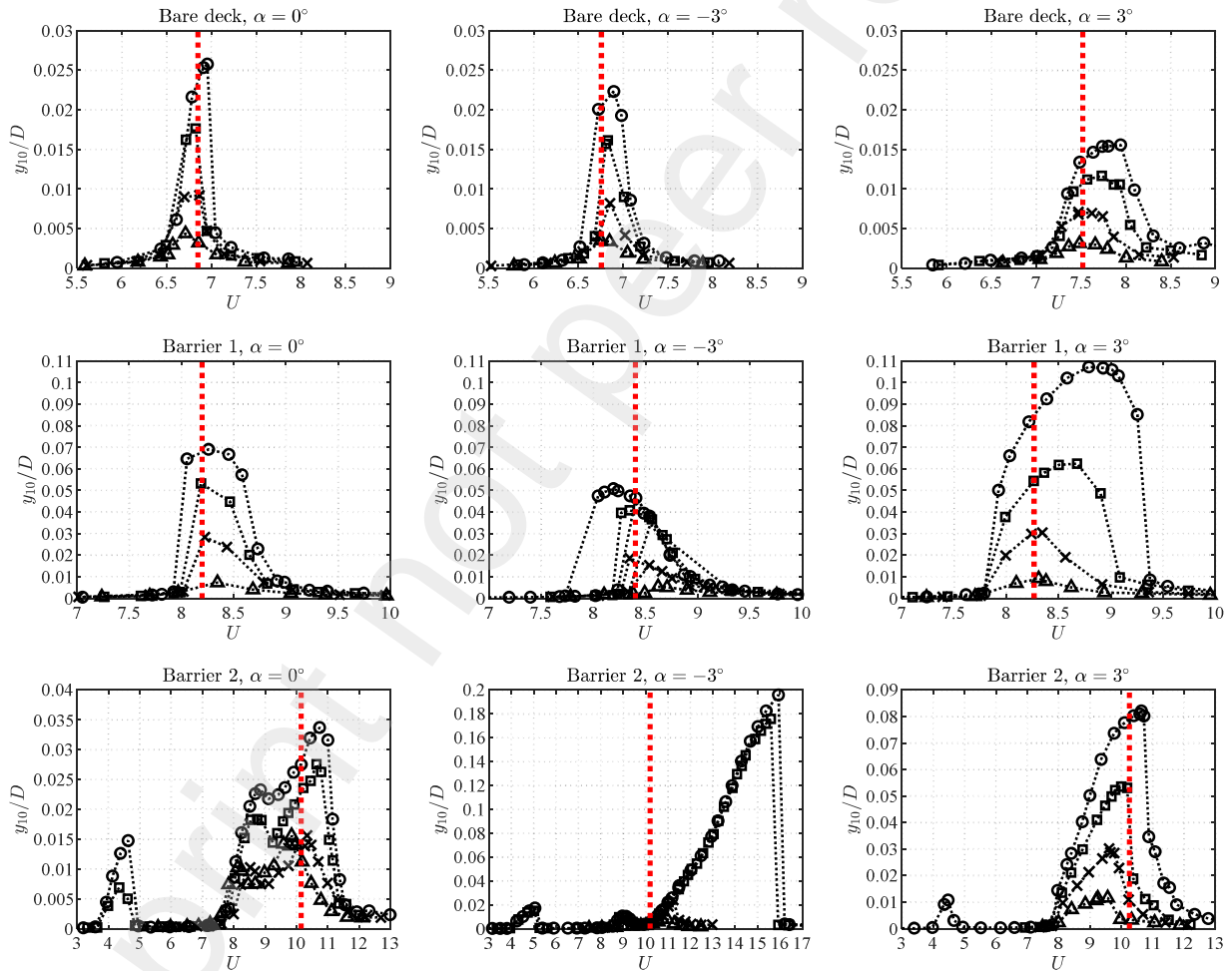


393
394 Fig. 11. Response curve for the deck equipped with Barrier 2 at $\alpha = -3^\circ$ for three different Scruton numbers.
395

396 Table 3. Scruton numbers related to the curves reported in Fig. 12 for each geometric layout and angle of attack.

	α [°]	Sc [-]			
		Sc_1	Sc_2	Sc_3	Sc_4
		⊙	■	×	△
Bare deck	0	3.2	7.7	19.6	53.6
	-3	3.0	8.2	19.5	51.8
	3	3.3	7.5	17.5	50.6
Barrier 1	0	3.5	7.2	18.9	59.2
	-3	3.8	6.7	20.7	58.7
	3	3.4	12.2	29.5	62.2
Barrier 2	0	3.8	7.9	20.5	65.2
	-3	3.9	4.9	12.7	60.7
	3	3.5	12.5	28.2	59.9

397



398 Fig. 12. Response curves for the bare deck and for the deck equipped with lateral barriers for the angles of attack 0°,
 399 -3° and 3° and four Scruton number values tested (see Table 3 for the values and the markers). The vortex-resonance
 400 reduced velocity based on static test results, $1/St$, is indicated by the red dashed line.
 401

402 3.3 *Wake-velocity measurements*

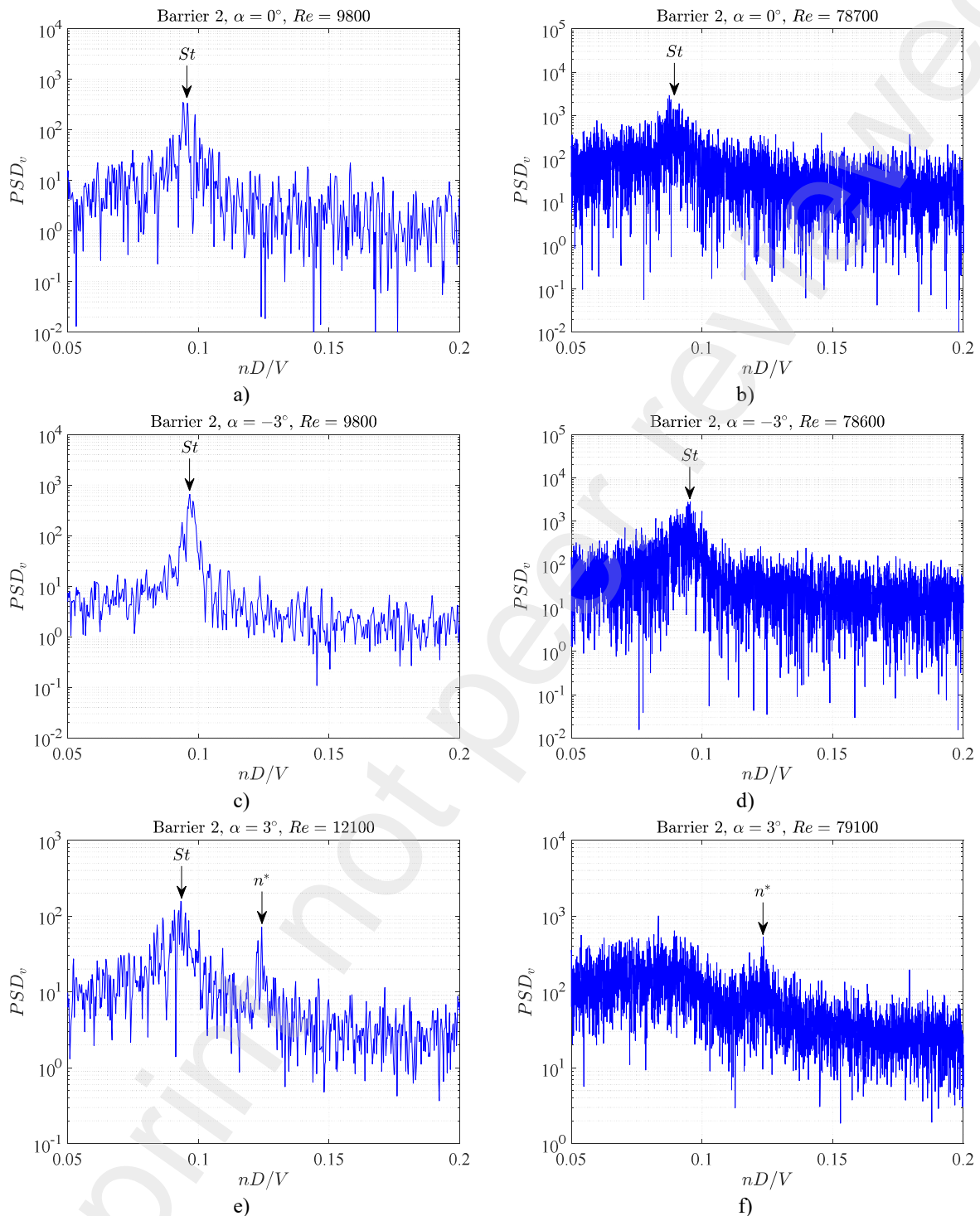
403 Flow-velocity measurements are carried out to examine in depth the vortex-shedding charac-
404 teristics for the deck equipped with Barrier 2, which showed the most peculiar VIV features. Wind
405 velocity fluctuations are measured through a hot-wire anemometer in a plane perpendicular to the
406 bridge model axis, while the latter is held fixed.

407 Fig. 13 shows the power spectral density of the velocity fluctuation for the probe located at
408 position P1 (Fig. 6) for the angles of attack 0° , -3° and 3° and different Reynolds numbers. The
409 Strouhal peak, corresponding to the one detected through force measurements, is indicated in the
410 figures, and no other narrow-band excitation at higher frequencies can be observed for $\alpha = 0^\circ$ and
411 -3° at both low and high Re . In contrast, two different narrow-band contributions can be identified
412 for $\alpha = 3^\circ$. The first peak corresponds to the Strouhal frequency found with force measurements
413 (named St), while the second, less energetic, peak occurs at a higher normalized frequency (named
414 n^*). They are both clearly visible for low Reynolds numbers (Fig. 13(e)), while they are less sharp
415 for high Reynolds numbers (Fig. 13(f)). The nondimensional frequency n^* is equal to 0.124 if
416 normalized with the bare deck depth D , but it becomes 0.58 if the deck width B is used for the
417 normalization.

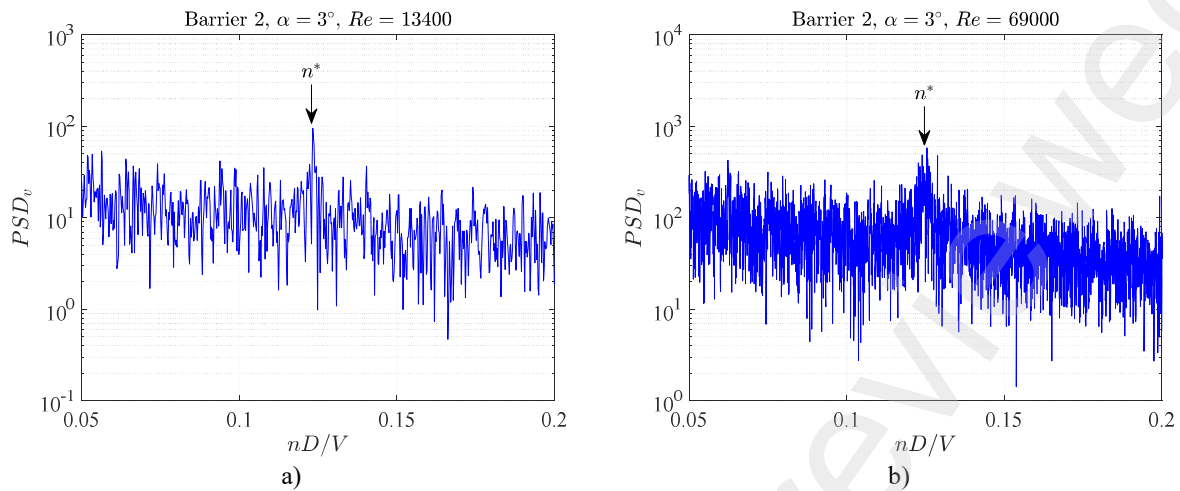
418 For $\alpha = 3^\circ$, the tests are repeated with the probe in the position P2, close to the leeward barrier
419 (Fig. 6). In this case, the Strouhal peak is visible neither at low nor at high Re , while n^* can still be
420 observed (Fig. 14). Therefore, coherent structures at the nondimensional frequency St does not
421 occur in the flow field very close to the deck upper-side, where only the mechanism related to n^*
422 develops.

423 In conclusion, wake measurements suggest the coexistence of two vortex-excitation mecha-
424 nisms for the deck equipped with Barrier 2 at an angle of attack of 3° . The peak detected at the
425 nondimensional frequency n^* can reasonably be associated with impinging shear-layer instability,
426 since $n^* = 0.58$ (normalized with B) is close to a value of about 0.6, observed by Nakamura and
427 Nakashima (1986) for an H-shaped section, a T-shaped section and rectangular cylinders over a
428 wide range of side ratios. On the other hand, the spectral peak related to the dimensionless fre-
429 quency St might be associated with a Kármán-vortex excitation, probably promoted by the inter-
430 action behind the bridge deck of the shear layer separating from the lower side of the section and
431 the vorticity overpassing the leeward traffic barrier.

432



433 Fig. 13. Power spectral density of the flow-velocity measurements at position P1 (see Fig. 6) for the sectional model
 434 equipped with Barrier 2 and for an angle of attack of 0° (a, b), -3° (c, d) and 3° (e, f). Results refer to the model held
 435 stationary at two different Reynolds numbers.

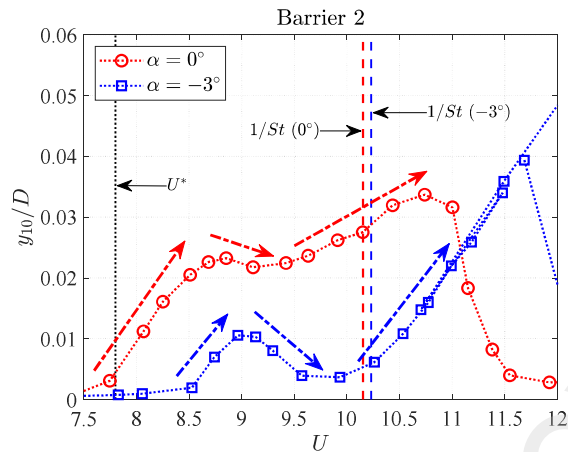


436 Fig. 14. Power spectral density of the flow-velocity measurements at position P2 (see Fig. 6) for the sectional model
 437 equipped with Barrier 2 and for an angle of attack of 3° . Results refer to the model held stationary at two different
 438 Reynolds numbers.

439 4 DISCUSSION

440 4.1 *Competing VIV excitation mechanisms*

441 An increase of the susceptibility to VIV of a bridge section is usually expected reducing the
 442 porosity of the barriers (see, e.g., Yan et al., 2022). In this study, the decrease in porosity from
 443 Barrier 1 to Barrier 2 also led to dramatic qualitative changes in the response patterns and to several
 444 interesting features (Fig. 10(c)), such as a noticeable anticipation of the lock-in onset compared to
 445 the reduced velocity $1/St$ associated with the Strouhal number measured during static tests. A no-
 446 ticeable peculiarity in the lock-in curve generated by Barrier 2 is shown in Fig. 15 for angles of
 447 attack of -3° and 0° . The trends highlighted by the arrows, exhibiting a secondary peak response
 448 in the first part of the synchronization range, suggest the possible coexistence of two excitation
 449 mechanisms. Nevertheless, the wake measurements for the stationary body discussed in Section
 450 3.3 demonstrated the presence of two excitation mechanisms only for $\alpha = 3^\circ$. Therefore, to examine
 451 this feature more in depth, wake measurements are repeated for the bridge model free to vibrate
 452 and inspected based on vibration results.

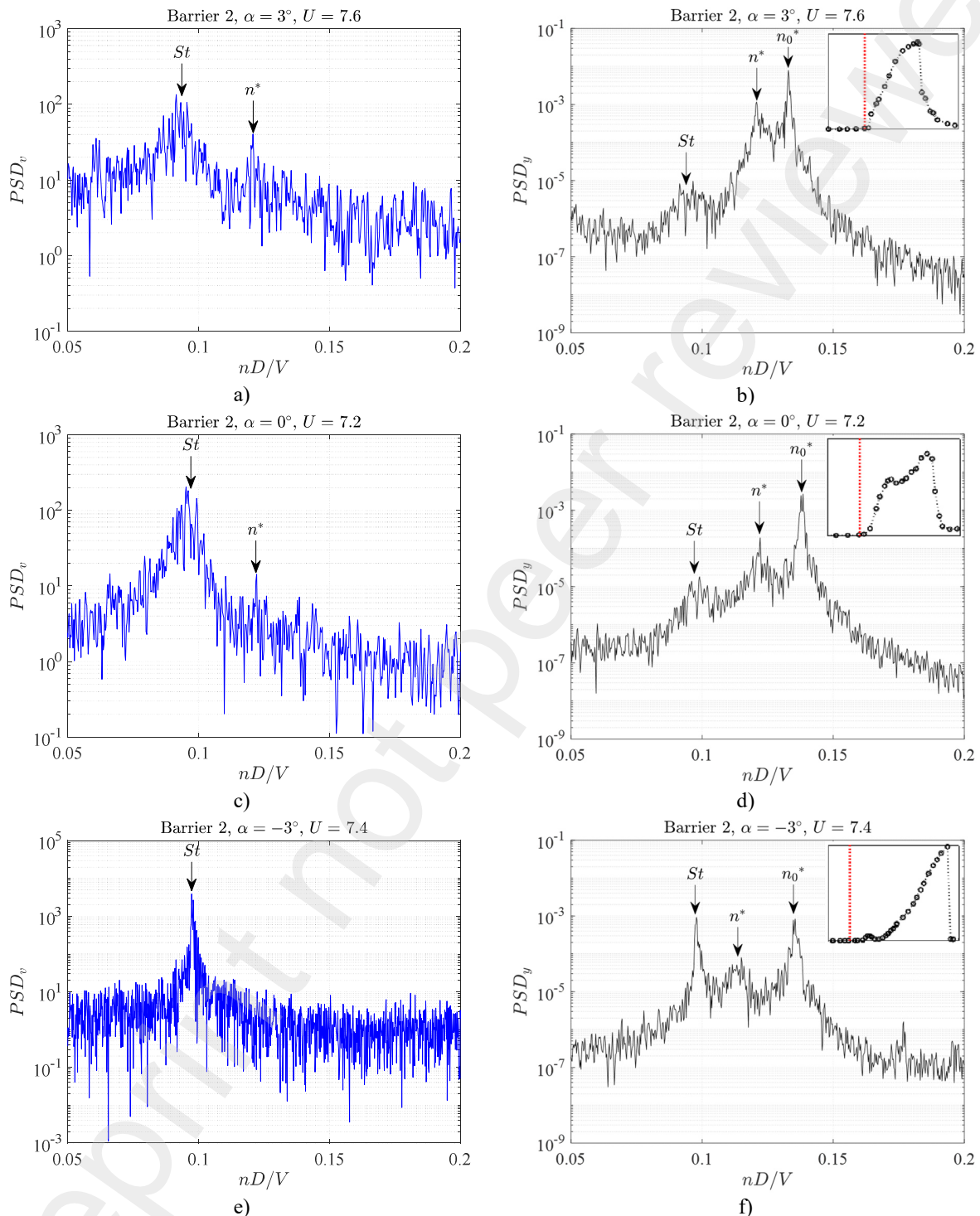


453

454 Fig. 15. Close up of the response curve between $U = 7.5$ and $U = 12$ for the deck equipped with Barrier 2 and angles
455 of attack of 0° and -3° .

456 Fig. 16 shows the power spectral density of both flow-velocity fluctuations (PSD_v) measured
457 in the wake of the model (position P1) and transverse vibrations (PSD_y), for a reduced velocity
458 slightly lower than the lock-in onset. For $\alpha = 3^\circ$, the coexistence of two contributions to the trans-
459 verse excitation observed for the stationary model (Fig. 13(c)) is confirmed in Fig. 16(a, b). The
460 values of St and n^* are the same as for the stationary case. The normalized natural frequency of the
461 system (n_0^*) is also indicated in the transverse vibration spectrum (Fig. 16(b)). The lock-in curve
462 exhibits a monotonic increase up to the peak response, with the abovementioned noticeable antic-
463 ipation of the onset compared to the resonance velocity associated with the frequency St . The in-
464 spection of the response spectra suggests that this can be ascribed to the synchronization between
465 the system and the vortex-excitation at frequency n^* , when the alleged Kármán-vortex shedding
466 frequency St is still quite far from the natural frequency; this is also the reason why in Fig. 16(b)
467 the peak corresponding to n^* is much higher than that associated with St . Therefore, two vortex-
468 excitation mechanisms clearly interact in the VIV response of the bridge.

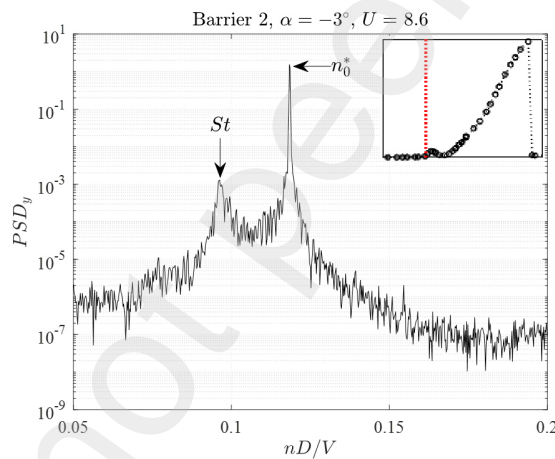
469 For a null angle of incidence, flow-velocity measurements in the wake of the model before the
470 lock-in onset (Fig. 16(c)) allow identifying a dominant peak St and a minor contribution at $n^* =$
471 0.122 (which becomes 0.57 if normalized with B). Both peaks are also visible in the transverse
472 displacement spectrum (Fig. 16(d)). In a similar way to what stated for $\alpha = 3^\circ$, the excitation at a
473 higher frequency n^* causes the clear anticipation of the lock-in onset compared to the Kármán-
474 vortex resonance reduced velocity $1/St$ inferred from static test results. The presence of two dif-
475 ferent excitation mechanisms also explains the lock-in pattern (Fig. 15), where two response curve
476 portions can clearly be distinguished in the synchronization range.



478 Fig. 16. Comparison between the power spectral density of the flow velocity at position P1 in the wake of the model
 479 equipped with Barrier 2 (a, c, e) and of the transverse vibration (b, d, f) for the considered angles of attack and a
 480 reduced velocity slightly lower than the lock-in onset (the Scruton number is between 3 and 4). The amplitude-velocity
 481 curves measured for the considered configurations are reported in the top-right box, where the dotted red line indicates
 482 the reduced velocity corresponding to the reported spectra.

483
484
485
486
487
488
489
490
491
492
493
494

Finally, for the negative angle of attack $\alpha = -3^\circ$, the wake flow velocity spectrum exhibits only a clear narrow-band peak at the frequency St (Fig. 16(e)), which is much more pronounced than in the previous two cases (as confirmed by the results reported in Table 2 and Fig. 13). Nevertheless, another small excitation contribution is visible in the displacement spectrum (Fig. 16(f)) at a reduced frequency of about 0.115 (0.53 if normalized with the deck width), indicated again as n^* in the figure. Fig. 17 shows that a weak synchronization regime occurs when n^* is very close to the natural frequency n_0^* , with the Kármán-vortex shedding peak still far from the resonance condition. Therefore, the small first part of the lock-in curve, over a reduced velocity range between 8.5 and 9.5 (Fig. 10(c), Fig. 11 and Fig. 15), is not promoted by the alleged Kármán-vortex shedding mechanism observed during static tests, but by a secondary excitation mechanism.



495
496
497
498

Fig. 17. Power spectral density of the transverse displacement of the model equipped with Barrier 2 at $\alpha = -3^\circ$ for a reduced velocity slightly higher than the onset of the first weak synchronization range, as indicated in the top-right box.

499
500
501
502
503
504
505
506

Therefore, when the model is free to vibrate, two vortex-shedding excitation mechanisms interact for all the three angles of attack considered, and not just for $\alpha = 3^\circ$ as one may have inferred from the results of static tests. As mentioned in Section 3.3, the secondary n^* -peaks are ascribable to impinging shear-layer instability, since its values are compatible with those reported by Nakamura and Nakashima (1986) and Naudascher and Wang (1993) for this phenomenon. This seems reasonable if one considers how the second typology of barriers modifies the bridge section geometry, with the solid lower portion of the barrier that promotes a sort of H-shape of the cross section. While for $\alpha = 3^\circ$ the intensity of the impinging shear-layer instability is sufficiently strong

507 to be observed even in stationary conditions, for $\alpha = 0^\circ$ and $\alpha = -3^\circ$ a slight vibration of the body
508 is necessary to trigger this secondary excitation mechanism. In this regard, it is worth noting that
509 Naudascher and Wang (1993) identified two different behaviors for stationary rectangular prisms:
510 for a side ratio between 2 and 8, the vortex formation is controlled by a mechanism equivalent to
511 the impinging-shear layer instability of flow past cavities (Rockwell and Naudascher, 1979), while
512 between 8 and 16 the same phenomenon is usually too weak to be identified without an external
513 trigger, such as a sound field (Stokes and Welsh, 1986) or a slight motion of the leading edge of
514 the body. Interestingly, in the present case study the ratio between the deck width and the solid
515 lower portion of the barrier is about 15.5.

516 According to Shiraishi and Matsumoto (1983), when Kármán-vortex excitation and impinging
517 shear-layer instability coexist, the onset of the lock-in curve is no longer strictly correlated with
518 the resonance reduced velocity $1/St$. By introducing a certain level of turbulence in the flow or a
519 splitter plate in the wake of a 4:1 rectangular cylinder and a hexagonal bridge section, Matsumoto
520 et al. (1993) demonstrate that the two mechanisms mutually disturb. In this way, the Kármán-
521 vortex shedding is reduced or suppressed, and the wind-induced vibration, driven only by the im-
522 pinging shear-layer instability, becomes larger. Based on this concept of competing mechanisms,
523 it seems reasonable in the present case that the largest oscillation amplitude occurs for $\alpha = -3^\circ$,
524 when the Kármán-vortex shedding mechanism is strongest and the impinging shear-layer instabil-
525 ity mechanism weakest (Fig. 13(c) and Fig. 16(e, f)). However, in this case, the dramatic drop of
526 the response for a slight increase in the Scruton number (Fig. 11) remains unexplained. In addition,
527 the presence of competing vortex-excitation mechanisms alone is not able to explain why the os-
528 cillation amplitudes are higher for $\alpha = 3^\circ$ than for $\alpha = 0^\circ$, since the strongest contribution from
529 impinging shear-layer instability is observed in the former case (Fig. 16(e)) but the peak oscillation
530 amplitude is also slightly larger. Nevertheless, this is not too surprising, considering the remarka-
531 bly different aerodynamics for the two angles of attack with Barrier 2 installed (Fig. 7) and the
532 higher intensity of Kármán-vortex shedding revealed by static tests for $\alpha = 3^\circ$ (see C_{L0} values in
533 Table 2).

534 Finally, the identification of two clear portions in the response curve, as in the current work for
535 $\alpha = 0^\circ$ and $\alpha = -3^\circ$, to the Authors' best knowledge, has been documented only in very few cases
536 in the literature. An example is provided by Matsumoto et al. (1993, 1999) for the torsional re-
537 sponse of a 4:1 rectangular cylinder: two local peak responses are identified at reduced velocities

538 corresponding to motion-induced and Kármán-vortex excitations, while only the peak associated
539 with the former mechanism is detected after installing a splitter plate, which also significantly
540 enhances the maximum response amplitude. Another example is represented by the low-speed
541 small response found by Mannini et al. (2016) for a 3:2 rectangular cylinder at low Scruton number
542 and ascribed to a weak resonance with a secondary mechanism of impinging shear-layer instabil-
543 ity.

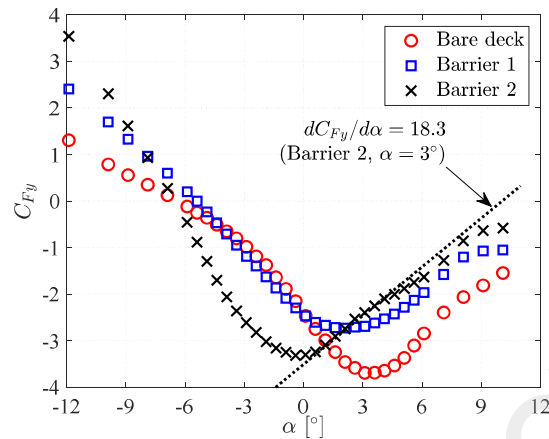
544 4.2 *Quasi-steady theory galloping predictions*

545 The transverse aerodynamic coefficient (C_{Fy}) for different angles of attack points out that, ac-
546 cording to the quasi-steady theory, some of the test cases considered are expected to exhibit gal-
547 loping instability in the velocity range explored during aeroelastic tests. In this regard, the trans-
548 verse force coefficient is reported in Fig. 18, evaluated based on static force measurements in the
549 following way:

$$C_{Fy}(\alpha) = -\sec(\alpha) [C_L(\alpha) + C_D(\alpha) \tan(\alpha)] \quad (1)$$

550 As expected, the effect of the lateral barriers on C_{Fy} is noticeable. In particular, for Barrier 2 and
551 $\alpha = 3^\circ$ the slope of the force coefficient is largely positive, suggesting a marked proneness to
552 galloping instability according to the Den Hartog criterion (Den Hartog, 1956). Transverse insta-
553 bility is here predicted, for the lowest mechanical damping tested, at a reduced velocity of about
554 $U = 2$, which is much lower than the vortex-resonance reduced velocity $1/St$. In this case, quench-
555 ing of the galloping instability may be expected up to the vortex-resonance velocity, followed by
556 the onset of a divergent instability (Parkinson and Wawzonek, 1981; Mannini et al., 2014, 2018).
557 In contrast, such instability was not observed during the aeroelastic tests (not even beyond the
558 wind speed range shown in Fig. 9(c)). Another example of mismatch with the quasi-steady theory
559 is encountered for the bare deck at $\alpha = 8.5^\circ$ (see Nicese, 2021), even if these results are not included
560 here for the sake of brevity.

561



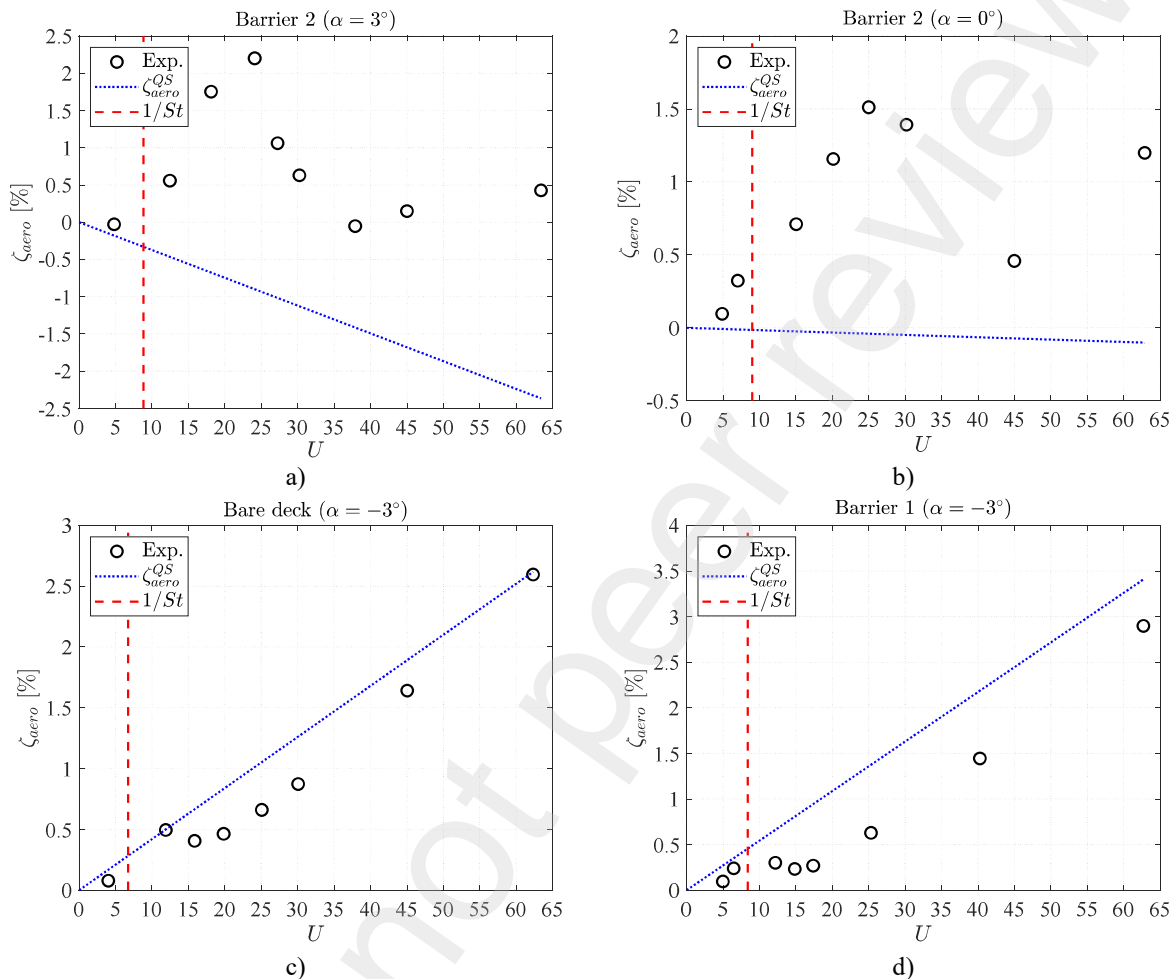
562
563 Fig. 18. Quasi-steady transverse force coefficient at different angles of attack for the sectional model with and without
564 barriers ($Re = 100,000$). The positive slope related to Barrier 2 at $\alpha = 3^\circ$ is indicated.

565 For a deeper investigation of this issue, experimental measurements of the aerodynamic damp-
566 ing (ζ_{aero}) are carried out by means of specific free-decay tests. The model installed on the aeroe-
567 lastic setup (Fig. 4(b)) is released from an initial condition of transverse displacement, and the
568 following oscillation time history is recorded. The aerodynamic damping is determined by the
569 difference between the total damping measured under wind and the mechanical damping in still
570 air. The tests are performed outside the lock-in range, both at low and at high reduced velocities,
571 since in the latter case the quasi-steady theory is expected to be more accurate. The measured
572 aerodynamic damping is then compared to the values predicted by the quasi-steady theory, evalu-
573 ated as follows:

$$\zeta_{aero}^{QS} = -\frac{\rho D^2 L}{8\pi M} \cdot \frac{dC_{Fy}}{d\alpha} \cdot U \quad (2)$$

574 Fig. 19 reports a selection of representative results, starting from the abovementioned case of
575 the deck with Barrier 2 at $\alpha = 3^\circ$. The experimental values are almost everywhere positive, in clear
576 contrast to the negative quasi-steady predictions (Fig. 19(a)). A similar result is obtained for the
577 deck equipped with Barrier 2 at null angle of attack (Fig. 19(b)), although in this case the negative
578 trend of the quasi-steady aerodynamic damping is very weak and instability is not predicted within
579 the reduced velocity range tested in the wind tunnel. In contrast, Fig. 19(c, d) reports two config-
580 urations (bare deck and deck equipped with Barrier 1, for an angle of attack of -3°), for which the
581 measurements exhibit a satisfying agreement with the quasi-steady theory, or at least an asymptotic

582 convergence is envisaged at very high reduced velocity. Interestingly, in these cases the quasi-
 583 steady predictions are reasonable even at low reduced velocity.
 584



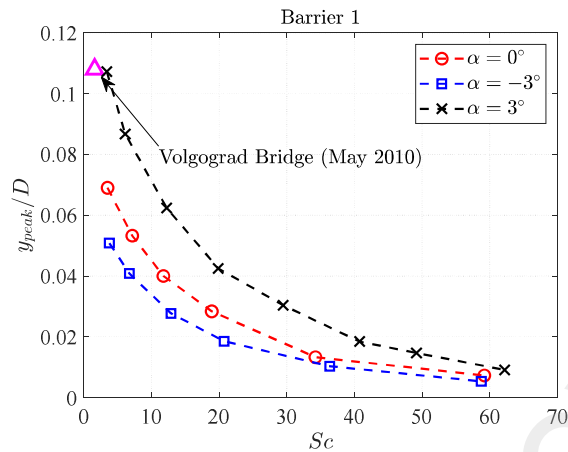
585 Fig. 19. Aerodynamic damping measured via free-decay tests for the deck equipped with Barrier 2 at $\alpha = 3^\circ$ (a) and at
 586 $\alpha = 0^\circ$ (b), for the bare deck at $\alpha = -3^\circ$ (c), and for the deck equipped with Barrier 1 at $\alpha = -3^\circ$ (d).

587 The qualitative discrepancy between the quasi-steady theory and the experimental evidence has
 588 already been observed in the literature for other geometries, such as for a square cylinder at an
 589 angle of attack of 12° (Carassale et al., 2015), and for a bridge trapezoidal open section at $\alpha = -4^\circ$
 590 (Chen et al., 2020), but a clear explanation for that has not been provided yet. Such an issue will
 591 deserve due attention in the future, even from a VIV response modeling perspective, since the
 592 quasi-steady theory is also employed in several VIV mathematical models to account for the aer-
 593 odynamic damping not associated with the vortex shedding (e.g., Tamura and Shimada, 1987;
 594 Marra et al., 2017; Mannini et al., 2018).

595 4.3 Comparison with the Volgograd Bridge response

596 A comparison between the experimental response of the sectional model considered in the pre-
597 sent work and that of the Volgograd Bridge, by which it is inspired, may be of interest. The infor-
598 mation about the incoming flow during the famous VIV event in 2010 is limited and mostly pro-
599 vided by Corriols and Morgenthal (2012), Weber et al. (2013), and Corriols (2015). The Volgograd
600 Bridge exhibited a violent lock-in for a wind velocity between 11.6 m/s and 15.6 m/s, which, for
601 a first bending frequency of 0.45 Hz and a cross-flow size of the bare deck of 3.61 m, leads to an
602 estimate of the Strouhal number between 0.104 and 0.140. The value of St for the sectional model
603 equipped with the Barrier 1 (fairly similar to that installed on the real bridge), is about 0.12 for an
604 angle of attack ranging from -3° to 3° (Table 2). The maximum vibration amplitude exhibited by
605 the bridge in May 2010 is about 40 cm, corresponding to 0.11 in dimensionless form (being nor-
606 malized with the deck depth). Fig. 20 reports the maximum vibration amplitude against the Scruton
607 number for the wind tunnel model, while the triangular marker refers to the Volgograd Bridge
608 prototype; for the latter, the estimate of the Scruton number is based on the data available in the
609 literature and on an assumed value of the structural damping of 0.003 according to EN 1991-1-4
610 (2010), since no information is available about this parameter. The peak response of the Volgograd
611 Bridge lays between the results obtained in the wind tunnel for $\alpha = 0^\circ$ and $\alpha = 3^\circ$.

612 However, as mentioned in Section 2.1, the wind tunnel model has a symmetric cross-section,
613 while the prototype bridge presents a pedestrian walkway only on one side. Moreover, the latter is
614 inclined of about 1° . Therefore, assuming a horizontal incoming flow, the relative angle of attack
615 would be equal to -1° . In addition, during the violent VIV event in 2010, the Volgograd Bridge
616 was exposed to a skew wind with respect to the bridge axis. All these uncertainties, along with
617 those affecting the Scruton number of the prototype, must be considered in the comparison re-
618 ported in Fig. 20. Despite this, the current wind tunnel campaign provides results that reasonably
619 comply with the full-scale observations.



620

621 Fig. 20. Dimensionless peak vibration amplitude against Scruton number for the sectional model equipped with Barrier
 622 1 and comparison with the estimate for the VIV event occurring in May 2010 for the Volgograd Bridge.

623 5 CONCLUSIONS

624 The present work deals with the VIV response of a non-streamlined box section, typically
 625 adopted for girder bridges, equipped with realistic traffic barriers and presenting a high ratio of
 626 barrier height to deck width and depth. The collection of literature works reported by Table 1 not
 627 only remarks the limited number of studies for this bridge family, but it also provides an extended
 628 and detailed database, which may be useful for further research dealing with bridge VIV response
 629 and effects of screens or barriers.

630 The current experimental study showed that the typology of barriers, along with small varia-
 631 tions in the angle of attack, can dramatically change the VIV response, not only in terms of vibra-
 632 tion amplitude, but also in terms of lock-in pattern. Partially solid traffic barriers or low-porosity
 633 pedestrian parapets (for instance, those realized in glass-like materials for aesthetic purposes) may
 634 even completely overturn the behavior of a non-streamlined section geometry, giving rise to a
 635 violent VIV response, incompatible with the bridge usage. This is particularly meaningful in view
 636 of the uncommon aerodynamic optimization of barriers other than for long-span cable-stayed and
 637 suspension bridges.

638 Low-porosity barriers, especially in presence of a continuous solid portion in contact with the
 639 deck surface (generating a cavity on the deck upper side), may promote impinging shear-layer
 640 instability. The interaction between the two mechanisms of excitation may not be detected through
 641 static tests, commonly employed to determine the Strouhal number of a bridge section. From the

642 engineering practice point of view, this may result in a significant anticipation of the lock-in onset
643 compared to the predictions based on the Strouhal number. Kármán-vortex shedding and imping-
644 ing shear-layer instability seem to interfere and disturb each other; indeed, the largest VIV re-
645 sponse with the less-porous barrier is observed for the angle of attack for which the second mech-
646 anism is weakest. In some cases, multiple excitation mechanisms are even inferable from the lock-
647 in curve morphology.

648 Finally, the current results highlight the failure of the quasi-steady theory in predicting trans-
649 verse divergent instabilities for some of the considered test cases, as confirmed by the direct meas-
650 urement of the aerodynamic damping at high reduced wind speed. Such a behavior, already en-
651 countered in the literature for other bluff cross sections, has not been explained yet and represents
652 an important open issue, even from the perspective of VIV modeling.

653 REFERENCES

- 654 Bai, H., Ji, N., Xu, G., & Li, J. (2020). An alternative aerodynamic mitigation measure for
655 improving bridge flutter and vortex induced vibration (VIV) stability: Sealed traffic barrier.
656 *Journal of Wind Engineering and Industrial Aerodynamics*, 206, 104302.
- 657 Bartoli, G., Contri, S., Mannini, C., & Righi, M. (2009). Toward an improvement in the
658 identification of bridge deck flutter derivatives. *Journal of Engineering Mechanics*, 135(8),
659 771-785.
- 660 Battista, R. C., & Pfeil, M. S. (2000). Reduction of vortex-induced oscillations of Rio-Niterói
661 bridge by dynamic control devices. *Journal of Wind Engineering and Industrial
662 Aerodynamics*, 84, 273-288.
- 663 Carassale, L. F. (2015). Motion-excited forces acting on a square prism: a qualitative analysis.
664 *Proceedings of 14th International Conference on Wind Engineering*. Porto Alegre, Brazil.
- 665 Chen, C., Mannini, C., Bartoli, G., & Thiele, K. (2020). Experimental study and mathematical
666 modeling on the unsteady galloping of a bridge deck with open cross section. *Journal of
667 Wind Engineering and Industrial Aerodynamics*, 203, 104170.
- 668 Chen, Z., Liu, S., Yu, X., Ma, C., & Liu, L. (2017). Experimental Investigations on VIV of Bridge
669 Deck Sections: A Case Study. *KSCE Journal of Civil Engineering*.

- 670 Corless, R. M., & Parkinson, G. V. (1988). A model of the combined effects of vortex-induced
671 oscillation and galloping. *Journal of Fluids and Structures*, 2, 203-220.
- 672 Corriols, A. S. (2015). Vortex-induced vibrations on bridges. The interaction mechanism in
673 complex sections and a new-proposed semi-empirical model. Ph.D. Thesis, Technical
674 University of Madrid, Madrid, Spain.
- 675 Corriols, A. S., & Morgenthal, G. (2012). Computational analysis of VIV observed on existing
676 bridges. *Proceedings of The Seventh International Colloquium on Bluff Body
677 Aerodynamics and Applications (BBAA7)*. Shanghai, China.
- 678 Den Hartog, J. P. (1956). *Mechanical Vibrations*. 4th ed., McGraw-Hill, New York. Reprinted by
679 Dover, New York, 1984.
- 680 Ehsan, F., & Scanlan, R. H. (1990). Vortex-induced vibrations of flexible bridges. *Journal of
681 Engineering Mechanics*, 116(6), 1392-1411.
- 682 Eurocode 1 (2005), Actions on structures - General actions. Part 1-4: Wind actions, CEN, EN
683 1991-1-4. (Corrigendum, January 27, 2010).
- 684 Frandsen, J. B. (2001). Simultaneous pressures and accelerations measured full-scale on the Great
685 Belt East suspension bridge. *Journal of Wind Engineering and Industrial Aerodynamics*,
686 89, 95-129.
- 687 Fujino, Y., & Yoshida, Y. (2002). Wind-Induced Vibration and Control of Trans-Tokyo Bay
688 Crossing Bridge. *Journal of Structural Engineering*, 128, 1012-1025.
- 689 Ge, Y., Zhao, L., & Cao, J. (2022). Case study of vortex-induced vibration and mitigation
690 mechanism for a long-span suspension bridge. *Journal of Wind Engineering and Industrial
691 Aerodynamics*, 220(104866).
- 692 Honda, A., Ito, M., & Kimura, H. (1992). Aerodynamic Instability of Prestressed Concrete Cable-
693 stayed Bridge with Noise Barrier. *Journal of Wind Engineering and Industrial
694 Aerodynamics*, 41-44, 1169-1180.
- 695 Hu, C., Zhao, L., & Ge, Y. (2018). Time-frequency evolutionary characteristics of aerodynamic
696 forces around a streamlined closed-box girder during vortex-induced vibration. *Journal of
697 Wind Engineering & Industrial Aerodynamics*, 182, 330-343.
- 698 Hwang, Y. C., Kim, S., & Kim, H. K. (2019). Cause investigation of high-mode vortex-induced
699 vibration in a long-span suspension bridge. *Structure and Infrastructure Engineering*, 16,
700 84-93.

- 701 Kubo, Y., Kimura, K., Sadashima, K., Okamoto, Y., Yamaguchi, E., & Kato, K. (2002).
702 Aerodynamic performance of improved shallow π shape bridge deck. *Journal of Wind*
703 *Engineering and Industrial Aerodynamics*, 90, 2113-2125.
- 704 Kumarasena, T., Scanlan, R. H., & Ehsan, F. (1991). Wind-Induced Motions of the Deer Isle
705 Bridge. *Journal of Structural Engineering*, 117, 3356-3374.
- 706 Larose, G. L., Larsen, S. V., Larsen, A., Hui, M., & Jensen, A. G. (2003). Sectional model
707 experiments at high Reynolds number for the deck of a 1018 m span cable-stayed bridge.
708 *Proceedings of 11th International Conference on Wind Engineering*, (pp. 373-380).
709 Lubbock, TX, USA.
- 710 Larsen, A. (1993). Aerodynamic aspects of the final design of the 1624 m suspension bridge across
711 the Great Belt. *Journal of Wind Engineering and Industrial Aerodynamics*, 48, 261-285.
- 712 Larsen, A., & Wall, A. (2012). Shaping of bridge box girders to avoid vortex shedding response.
713 *Journal of Wind Engineering and Industrial Aerodynamics*, 104-106, 159-165.
- 714 Larsen, A., Eisdahl, S., Andersen, J. E., & Vejrum, T. (2000). Storebælt suspension bridge - vortex
715 shedding excitation and mitigation by guide vanes. *Journal of Wind Engineering and*
716 *Industrial Aerodynamics*, 88, 283-296.
- 717 Larsen, A., Savage, M., Lafrenière, A., Hui, M. C., & Larsen, S. V. (2008). Investigation of vortex
718 response of a twin box bridge section at high and low Reynolds numbers. *Journal of Wind*
719 *Engineering and Industrial Aerodynamics*, 96, 934-944.
- 720 Larsen, A., Svensson, E., & Andersen, H. (1995). Design aspects of tuned mass dampers for the
721 Great Belt East Bridge approach spans. *Journal of Wind Engineering and Industrial*
722 *Aerodynamics*, 54/55, 413-426.
- 723 Li, M., Sun, Y., Jing, H., & Li, M. (2018). Vortex-Induced Vibration Optimization of a Wide
724 Streamline Box Girder by Wind Tunnel Test. *KSCE Journal of Civil Engineering*, 22(12),
725 5145-5153.
- 726 Macdonald, J. H., A., I. P., & Fletcher, M. S. (2002). Vortex-induced vibrations of the Second
727 Severn Crossing cable-stayed bridge - full-scale and wind tunnel measurements.
728 *Proceedings of the Institution of Civil Engineers - Structures and Buildings*, 152, pp. 123-
729 134.

- 730 Mannini, C., Marra, A. M., & Bartoli, G. (2014). VIV-galloping instability of rectangular
731 cylinders: Review and new experiments. *Journal of Wind Engineering and Industrial*
732 *Aerodynamics*, 132, 109-124.
- 733 Mannini, C., Marra, A. M., Massai, T., & Bartoli, G. (2016). Interference of vortex-induced
734 vibration and transverse galloping for a rectangular cylinder. *Journal of Fluids and*
735 *Structures*, 66, 403-423.
- 736 Mannini, C., Marra, A. M., Pigolotti, L., & Bartoli, G. (2017). The effects of free-stream turbulence
737 and angle of attack on the aerodynamics of a cylinder with rectangular 5:1 cross section.
738 *Journal of Wind Engineering and Industrial Aerodynamics*, 161, 42-58.
- 739 Mannini, C., Massai, T., & Marra, A. M. (2018). Modeling the interference of vortex-induced
740 vibration and galloping for a slender rectangular prism. *Journal of Sound and Vibration*,
741 419, 493-509.
- 742 Mannini, C., Massai, T., & Marra, A. M. (2018). Unsteady galloping of a rectangular cylinder in
743 turbulent flow. *Journal of Wind Engineering and Industrial Aerodynamics*, 173, 210-226.
- 744 Marra, A. M., Mannini, C., & Bartoli, G. (2011). Van der Pol-type equation for modeling vortex-
745 induced oscillations of bridge decks. *Journal of Wind Engineering and Industrial*
746 *Aerodynamics*, 99(6-7), 776-785.
- 747 Marra, A. M., Mannini, C., & Bartoli, G. (2015). Measurements and improved model of vortex-
748 induced vibration for an elongated rectangular cylinder. *Journal of Wind Engineering and*
749 *Industrial Aerodynamics*, 145, 358-367.
- 750 Marra, A. M., Mannini, C., & Bartoli, G. (2017). Modeling of vortex-induced vibrations of an
751 elongated rectangular cylinder through wake-oscillator models. *Proceedings of the 7th*
752 *European and African Conference on Wind Engineering*. Liège, Belgium.
- 753 Matsumoto, M., Shiraishi, N., Shirato, H., Stoyanoff, S., & Yagi, T. (1993). Mechanism of, and
754 turbulence effect on vortex-induced oscillations for bridge box girders. *Journal of Wind*
755 *Engineering and Industrial Aerodynamics*, 49, 467-476.
- 756 Matsumoto, M., Shirato, H., Yagi, T., Shijo, R., Eguchi, A., & Tamaki, H. (2003). Effects of
757 aerodynamic interferences between heaving and torsional vibration of bridge decks: the
758 case of Tacoma Narrows Bridge. *Journal of Wind Engineering and Industrial*
759 *Aerodynamics*, 1547-1557.

- 760 Meng, X., Zhu, L., & Guo, Z. (2011). Aerodynamic interference effects and mitigation measures
761 on vortex-induced vibrations of two adjacent cable-stayed bridges. *Frontiers of*
762 *Architecture and Civil Engineering in China*, 5(4), 510-517.
- 763 Nakamura, Y., & Matsukawa, T. (1987). Vortex excitation of rectangular cylinders with a long
764 side normal to the flow. *Journal of Fluid Mechanics*, 180, 171-191.
- 765 Nakamura, Y., & Nakashima, M. (1986). Vortex excitation of prisms with elongated rectangular,
766 H and I cross-sections. *Journal of Fluid Mechanics*, 163, 149-169.
- 767 Naudascher, E., & Wang, Y. (1993). Flow-induced vibrations of prismatic bodies and grids of
768 prisms. *Journal of Fluids and Structures*, 7, 341-373.
- 769 Nicese, B. (2021). Influence of Cross-Section Details on Vortex-Induced Vibrations of Bridge
770 Decks: Experiments and Modeling. Ph.D. Thesis, University of Florence, Florence, Italy.
- 771 Owen, J. S., Vann, A. M., Davies, J. P., & Blakeborough, A. (1996). The prototype testing of
772 Kessock Bridge: response to vortex shedding. *Journal of Wind Engineering and Industrial*
773 *Aerodynamics*, 60, 91-108.
- 774 Piccardo, G., Carassale, L., & Freda, A. (2011). Critical conditions of galloping for inclined square
775 cylinders. *Journal of Wind Engineering and Industrial Aerodynamics*, 99, 748-756.
- 776 Ricciardelli, F., de Grenet, E. T., & Hangan, H. (2002). Pressure distribution, aerodynamic forces
777 and dynamic response of box bridge sections. *Journal of Wind Engineering and Industrial*
778 *Aerodynamics*, 1135-1150.
- 779 Rockwell, D., & Naudascher, E. (1978). Self-Sustaining Oscillations of Flow Past Cavities.
780 *Journal of Fluids Engineering*, 100, 152-165.
- 781 Sarwar, M. W., & Ishihara, T. (2010). Numerical study on suppression of vortex-induced
782 vibrations of box girder bridge section by aerodynamic countermeasures. *Journal of Wind*
783 *Engineering and Industrial Aerodynamics*, 98, 701-711.
- 784 Schewe, G. (1989). Nonlinear flow-induced resonances of an H-shaped section. *Journal of Fluids*
785 *and Structures*, 327-348.
- 786 Schewe, G., & Larsen, A. (1998). Reynolds number effects in the flow around a bluff bridge deck
787 cross section. *Journal of Wind Engineering and Industrial Aerodynamics*, 74-76, 829-838.
- 788 Seo, J. W., Kim, H. K., Park, J., Kim, K. T., & Kim, G. N. (2013). Interference effect on vortex-
789 induced vibration in a parallel twin cable-stayed bridge. *Journal of Wind Engineering and*
790 *Industrial Aerodynamics*, 116, 7-20.

- 791 Shiraishi, N., & Matsumoto, M. (1983). On classification of vortex-induced oscillation and its
792 application for bridge structures. *Journal of Wind Engineering and Industrial*
793 *Aerodynamics*, 14, 419-430.
- 794 Stokes, A. N., & Welsh, M. C. (1986). Flow-resonant sound interaction in a duct containing a
795 plate, II: Square leading edge. *Journal of Sound and Vibration*, 104, 55-73.
- 796 Sun, Y., Li, M., Li, M., & Liao, H. (2019). Spanwise correlation of vortex-induced forces on
797 typical bluff bodies. *Journal of Wind Engineering and Industrial Aerodynamics*, 189, 186-
798 197.
- 799 Tamura, Y., & Shimada, K. (1987). A mathematical model for the transverse oscillations of square
800 cylinders. *Proceedings of the 1st International Conference on Flow Induced Vibrations*,
801 (pp. 267-276). Bowness-on-Windermere, UK.
- 802 Wang, X., Xu, F., Zhang, Z., Wang, Y., & Zhang, M. (2023). Numerical explorations of the vortex-
803 induced vibration of a streamlined box girder with water-filled barriers. *Journal of Wind*
804 *Engineering and Industrial Aerodynamics*, 240, 105496.
- 805 Wang, Y., Chen, X., & Li, Y. (2020). Nonlinear self-excited forces and aerodynamic damping
806 associated with vortex-induced vibration and flutter of long span bridges. *Journal of Wind*
807 *Engineering and Industrial Aerodynamics*, 204, 104207.
- 808 Weber, F., Distl, J., & Maślanka, M. (2013). Semi-Active TMD Concept for Volgograd Bridge.
809 *Proceedings of the 31st IMAC, A Conference on Structural Dynamics*, (pp. 79-88).
- 810 Yan, Y., Yagi, T., Noguchi, K., Ito, Y., & Shimada, R. (2022). Effects of Handrail Details on
811 Vortex-Induced Vibration for a Box-Girder Bridge. *Journal of Bridge Engineering*, 27(3),
812 04021114.
- 813 Zhu, L. D., Meng, X. L., & S., G. Z. (2013). Nonlinear mathematical model of vortex-induced
814 vertical force on a flat closed-box bridge deck. *Journal of Wind Engineering and Industrial*
815 *Aerodynamics*, 69-82.
- 816